POLYTECHNIC UNIVERSITY OF
CATALONIA, UPC

MASTER THESIS

Development of a numerical model for the transport of dust

Author:
Yuyang WANG

Supervisor:
Dr. Joan BAIGES
Prof. Ramon CODINA

A thesis submitted in fulfillment of the requirements for the degree of Master of Science

in the

Fluid mechanics group
Department of Civil and Environmental Engineering
Polytechnic University of Catalonia, UPC

June 15, 2017

Declaration of Authorship

I, Yuyang WANG, declare that this thesis titled, "Development of a numerical model for the transport of dust" and the work presented in it are my own. I confirm that:

- This work was done wholly or mainly while in candidature for a master degree at this University.
- Where any part of this thesis has previously been submitted for a degree or any other qualification at this University or any other institution, this has been clearly stated.
- Where I have consulted the published work of others, this is always clearly attributed.
- Where I have quoted from the work of others, the source is always given. With the exception of such quotations, this thesis is entirely my own work.
- I have acknowledged all main sources of help.
- Where the thesis is based on work done by myself jointly with others, I have made clear exactly what was done by others and what I have contributed myself.

Signed:

Date:

"If the facts don't fit the theory, change the facts."

Albert Einstein

Polytechnic University of Catalonia, UPC

Abstract

International Center for Numerical Methods in Engineering

Department of Civil and Environmental Engineering

Master of Science

Development of a numerical model for the transport of dust

by Yuyang WANG

This master thesis focuses on the development of an numerical model to simulate the transport of dust particles eroded from land surface and convected by wind flow.

The first part of this thesis is the literature review about existing methods to model the transport of dust particles. Analytical methods may produce some solution on given condition while numerical solution may extended to an even wider application with arbitrary boundary conditions appearing naturally. Based on these methods, the erosion mechanism is that once the friction velocity lager than the threshold friction velocity, particles are generated and entering the air becoming free particles which can be convected by wind flow.

The second part is another core of this thesis, where we focus on the finite element methods to solve the mathematical model proposed for the dust transport. Special techniques have been introduced considering the convection dominated cases which will cause unstable solutions of the problem, while the shock capturing method are also used to eliminate the the local oscillations appearing in regions where solution has sharp gradient.

In the last part we implement our model in FEMUSS, which is a multiphysics simulation software written in Fortran 2003. Specified cases are designed in order to verify the effectiveness of the code and model. Numerical tests show that our model works very well and gives more accurate solutions. The mechanism found in the experiments can be reproduced by our numerical solution. In order to take advantage of numerical methods, we also present a real application of our model trying to simulate the dust transport in a large wind tunnel, where we can see the concentration dynamics evolve with time.

Acknowledgements

I still remember the first email I sent to Prof.Ramon Codina to ask if he had projects for my master thesis. He was very generous and responded me in the next day, providing me with five topics which I could choose. With the careful explanation from Dr.Joan Baiges, I finally decided to do the current one. And of course, they are my final supervisors for the thesis. Because I do not have solid foundation in mathematics, I suffered a lot from formulas in the literature. So here I want to use the opportunity to express my gratitude to Prof.Ramon Codina who alway explains theoretical knowledge with patience to me. I adore his greatest contribution to the development of fluid mechanics. I appreciate also Dr. Joan Baiges who gave me a lot of help especially about how to start the work, how to implement the model and how to do numerical tests. I gain knowledge about Fortran programing language from his FEMUSS software which is a masterpiece as a mulitiphysics simulation environment. I deeply thank them again for their guidance and being always accessible.

These months spent in fluid mechanics group, I have enjoyed the accompany of many wonderful and helpful people in the C1-102 office. Laura, Vahid and Arnau are excellent PhD candidates and they always give me a hand when I need them. I should thank Camilo who gave me the first lecture on FEMUSS in the beginning. I would like to show my great gratitude to the secretary Lelia and the master coordinator Antonia who gave me many supports either small or big during my master studies.

When I came first to Barcelona, I knew nobody and quite didn't know what to expect for this new journey, but this generous and beautiful city surprised me with its people and live atmosphere. The long list of all the friends I've made here is too long, but I enjoyed friendship and accompany of a big group of people from very diverse backgrounds and countries. Christian and Jordi were just two of the best ones I have met in the class and we always study together. I hope we could maintain the friendship and keep in touch in the future.

I would also like to thank the joint scholarship which I obtained from *Universitat Politècnica de Catalunya* and *China Scholarship Council* so I do not have to worry about the financial issues and could focus on study here.

I would finally like to specially thank my parents, my sister and Qiyuan. They were the ones that encouraged me to solve the difficult problems I encountered during my master studies and supported me always.

Contents

List of Figures

List of Tables

List of Abbreviations

TCDR	**T**ransient **C**onvection **D**iffusion **R**eaction
NS	**N**avier **S**tokes
PDEs	**P**artial **D**ifferential **E**quation**s**
SUPG	**S**treamline **U**pwind **P**etrov **G**alerkin
GLS	**G**alerkin **L**east **S**quare
SGS	**S**ub**g**rid **S**cale

Chapter 1

Introduction

In atmospheric science, researchers have paid much attention to dust especially like aerosols because of their modification of the photochemical process, which holds the key to the atmospheric radiation related to the earth's radiative budget for investigating the climate change. Aerosols are usually generated from two main sources and finally could affect the global climate change: 1) the anthropogenic sources of aerosols including fossil fuel emissions, biomass burning and other agricultural or industrial activities; 2) the natural sources of aerosols derived from the sea salt and surface dust emissions[1]. These resuspended dust not only affects the atmospheric radiation, but also causes injury to sensitive plants and reduce visibility in the air.

In civil and environmental engineering, there is an increasing interest in mineral dust in the atmosphere and the corresponding negative impacts. The prerequisite for studying these impacts of aeolian dust is to determine the spatial distribution of dust concentration and its temporal variations. However, although numerous studies[2, 3, 4] have found some quantitative relationship in this subject, a complete model in terms of fluid dynamics has not been proposed yet. This is because the processes of dust emission and transport are very complex and difficult to model. Precisely, dust emission depends on an interactive set of physical processes governed by many factors such as climate like high wind and low rainfall, soil property (like soil composition, texture, aggregation and crusting), and surface roughness (like non-erodible elements and vegetation), and integration of these parameters quantitatively is a cumbersome work. Some pollutants like aerosol and dust transport generated by wind erosion in the atmosphere are potentially dangerous because the high mobility of the smaller particulate would have adverse effects on human health.

In practical application, we are interested in particle size ranging from $0.1\mu\mathrm{m}$ to $100\mu\mathrm{m}$ because these particles plays an important role for air pollution and human health. For example, $PM10$ describes a particulate matter with diameter that is generally $10\mu\mathrm{m}$ or smaller; $PM2.5$ is also another particulate matter $2.5\mu\mathrm{m}$ or smaller. $PM10$ or $PM2.5$ make up a large proportion of dust that can be drawn deep into the lungs, and even worse, larger particles tend to be trapped in the nose, mouth or throat. Chemical properties vary depending on the sources of particles, but dust is not a particular chemical

substance but a classification of particles by size rather than chemical properties. So it is of significant importance that we pay attention to this group of dust.

The finite element method is a helpful tool to deal with the numerical simulation of multi-physics problems. However, the complexity of the partial differential equations(PDEs) found in the problem usually makes these equations to be solved with instabilities or oscillation within the computational domain. Special techniques are required to eliminate these unstable solutions. For the incompressible Navier-stokes equations, numerical instabilities arise from incompressibility constraint and the presence of convection dominant terms. On the other hand, the lack of diffusion term in the Galerkin discretization terms was firstly regarded as the instability source, so the first attempts were to add an extra diffusive term and were called the artificial viscosity terms. But these methods are not consistent, i.e. the exact solution of the continuous problem does not satisfy the perturbed problem, resulting in a loss of accuracy. So the first consistent formulation is the streamline upwind Petrov Galerkin method(SUPG); this method and many similar methods like Galerkin Least-squrare(GLS) and Sub-grid scale(SGS) try to stabilize the convection-diffusion equation by adding an extra stabilization term which is proportional to the residual.

1.1 Objective

The objective of the present thesis is to implement a gravitational model for the transport of particles in a fluid, and validate these models with some practical applications such as the simulation of ventilation in tunnels.

1.2 Structure of the work

Let us close the introduction describing the organization of the work.

In chapter 2 we discuss the dust transport phenomena in nature arising from many problems.Their dynamic behaviors are very important to human health and the environment. Small dust particles such as $PM10$ and $PM2.5$ in air may be drawn into the body with every breath directly physical or even be absorbed into blood. The mechanism of how dust particles affect human health is explained briefly and strategies that can be designed to remove or decrease their negative effect are presented.

In chapter 3 the analytical methods used to simulate the dust concentration are summarized. However, in a general cases, the analytical solution is impossible to find. Following the traditional research lines that can be found in references, the dust generation mechanism is analyzed, with important parameters such as the threshold velocity and the horizontal and vertical dust

flux in the computational domain. Finally, the dust transport model is given in terms of a group of transient Navier-Stokes equations and a convection-diffusion equation. The boundary conditions for the Navier-Stokes equations are flexible, which means that depending on the problem we would like to model, boundary conditions can be different. In the dust transport model, the settling velocity due to gravitational force is formulated and also the diffusion coefficient of dust particles in the flow medium.

In chapter 4 we focus on the numerical method to approximate the dust transport model. The Galerking finite element method is introduced for the spatial discretization of the PDEs while finite difference methods are used for the temporal discretization. However, in case of convection dominated flows, the stabilization method like the variational multi-scale method, GLS and SGS are required in order to eliminate the oscillations. These stabilized finite element formulations yield a globally stable solution but if there exist a large gradient of the solution, local instabilities could still appear and pollute the solution. The so-called shock capturing method is adopted in our problem.

In chapter 5 we implement our model in FEMUSS, which is a multiphysics simulation software written in Fortran 2003. Specific test cases are designed in order to verify the effectiveness of the code and model. Numerical tests show that our model works very well and gives more accurate solutions compared to those found in the literature. In order to show the advantage of numerical methods, in chapter 6 we present real application of our model trying to simulate the dust transport in a large wind tunnel,which shows the advantages of numerical simulation.

We close the work with chapter 7, where conclusions and further possible research lines are summarized.

Chapter 2

Dust transport in fluids

Dust particles usually appear as many other natural phenomena, coupled with and affected by other physical field. Partial differential equations make it possible to describe the corresponding problem in terms of conservation,of mass, momentum or energy, which provide a way for mathematical modeling. On the other hand, we notice especially the negative effect of dust particles on human health and environments, and explain how they cause severe harm to the economy and environment.

2.1 Coupled problem

In a real world, many physical problems are coupled, meaning the solution of one problem could be the parameter of another one. For example, the coupled convection-diffusion and Navier-Stokes equations has many applications. In bioscience and biology, the proteins (actin filament in cells and hemoglobin in bloods) are usually generated from small monomers (amino acid and polysaccharides), but these substances are convected by fluids in the living body[5]. So the convection-diffusion equation is adopted in order to describe the mass conservation during this process and also the Navier-Stokes equations are also introduced for the advection velocity field. Besides, in some circumstances, the Navier-Stokes problem that model the convective part of the problem is conditioned by the amount of substances, and in the other way around, substances are convected by the underlying Navier-Stokes problem.

Many physical phenomena are governed by PDEs, and these equations can be approximately solved by finite element methods, which results in a sparse nonlinear/linear system of equations to be solved via linear algebra. In fluid mechanics, the flow could present complex patterns when different conditions are applied. In most cases, we are interested in incompressible flow, with the Mach number smaller than 0.3.

2.2 Adverse effects of dust

Numerous factors may contribute to the effect of dust on human health and the environment [6] . Vehicles emit gases harmful to plants, especially nitrogen oxides and ethylene, and also oil droplets and solid particles, including those containing lead. Further particles are derived from abrasion of tyres, brake linings and clutch plates, and the road surface. Air movement over central reserves is highly turbulent and the effect on plants of turbulent wind, and of spray from wet road surfaces, may be exacerbated by the presence of suspended material[7]. Leaves of plants on central reserves of roads with high traffic density are covered with black deposits. The possible effects are discussed as below.

2.2.1 Health effects

Dust particles in the $PM10$ size range are commonly present in air and may be drawn into the body with every breath. For instance, in the lungs dust can have a direct physical effect or even be absorbed into blood; airborne particles, not only the PM10 fraction, may also be deposited in mouth, throat or nose and be ingested[8].

Dust can cause extreme damage to human health, but recent epidemiological research suggests that there is no threshold at which health effects do not occur[9]. Precisely, the health effects include[10]:

- Toxic effects by absorption of the toxic material into the blood, such as heavy metal elements like lead, cadmium and zinc.
- Allergic or hypersensitivity effects, e.g. some woods, flour grains and chemicals can be blown by air wind and finally cause damage to special populations.
- Bacterial and fungal infections from live organisms.
- Fibrosis and cancer, e.g. asbestos, quartz and chromates.
- Increased respiratory symptoms, aggravation of asthma and premature death. The risks are highest for sensitive groups such as the elderly and children.

In fact, all people are continuously exposed to some harmful extent except in special filtered environments. Exposure may be higher in urban and industrial areas due to increased number of sources. However, high levels may also occur in natural environments. There are many factors which may affect the health effects arising from exposure to dust[11]:

- The chemical composition and physical properties of the particles.
- The mass concentration of the airborne particles.

- The size of the particles (smaller particles may be associated with more adverse effects because they can be inhaled more deeply into the lungs).
- The duration of exposure (short or long term).

Knowing these factors, which play an important role in controlling the effect of dust particles, we shall see in next chapter how our simulation could show the concentration and lifespan of dust in a given domain.

2.2.2 Environmental effects

Dust particles in the air affect both the quality of the air and visibility[11]. Once the particulate matter float in the air, it generally will take a long time to settle[12] ,floating in the air as shown in figure 2.1. This happens especially for very fine and light dust such as $PM10$ and $PM2.5$, which are easily entrained into the air by wind or disturbances[13]. In a late stage, chemical changes may occur, as may reactions with other substances, depending on the composition of the particles[14]. The particulates may be washed from the air by rain or snow. When they settle on land they may settle permanently or be activated again.

FIGURE 2.1: Effects of dust particles on the environment

$PM10$ may affect animals in the same way as it affects humans. Particles in general, not specially $PM10$ or $PM2.5$, affect the aesthetics and utility of areas through visibility reduction and may affect buildings and vegetation. The specific effect of particles depends on their compositions, concentration and presence of other pollutants such as acid forming gases[15].

Chapter 3

Mathematical Modeling of particle transport

In this chapter we discuss existing analytical methods developed to simulate the dust concentration in the atmosphere. However, analytical solutions of PDEs are limited to specific boundary conditions, and in order to have a model that can be expanded to any dust dynamics, we design a new mathematical model by coupling the transient convection-diffusion-reaction equation(TCDR) and Navier-Stokes equations, whose boundary conditions are flexible. Considering the effect of gravitational force, the dust deposition velocity is introduced to modify the convection terms in TCDR equation.

3.1 Analytical modeling

Due to the complexity of the problem itself,traditional methods trying to give analytical solutions are based on many simplifications or assumptions. We are going to introduce two models as a starting point of our model.

3.1.1 Gillette and Goodwin's model

One of the original studies on the particle concentration in the atmosphere is proposed by Gillette and Goodwin[16] who used an Eulerian Pasquill equation[17] as governing equation for the process:

$$\frac{\partial c}{\partial t} + \nabla \cdot (c\boldsymbol{a}) = \nabla \cdot (D\nabla c) - \boldsymbol{w}_t \cdot \nabla c \tag{3.1}$$

where $c(x, y, z, t)$ is the mean concentration of dust particles such as sand or soil aerosol; $\boldsymbol{a}$ is the advection velocity of the wind or fluids; $\boldsymbol{w}_t$ is the settling velocity arising from the balance of forces acting on the particles; $D(x, y, z)$ is the spatial diffusion tensor.

Assuming a steady-state condition and the homogeneity of c in the x and y directions, Gillette and Goodwin finally simplified the model as a differential

equation in 1D,

$$\frac{\partial}{\partial z}(D_z\frac{\partial c}{\partial z}) - w\frac{\partial c}{\partial z} = 0 \tag{3.2}$$

where w_t is the settling velocity in $z-$direction; D_z is the diffusivity, $D_z = u_*kz$ (k is the von Karman constant). The equation can be solved after integration twice as,

$$\begin{cases} c(z) = c(z_0)(\frac{z}{z_0})^{-\xi} \\ \lim_{z\to\infty} c(z) = 0 \\ c(z)|_{z=z_0} = \text{constant} \end{cases} \tag{3.3}$$

where z_0 is the roughness height and define $\xi = \frac{w_t}{ku_*}$. Eq.3.3 is almost the first attempt to give analytical solution of the particle settling in fluids. However, this is not accurate enough due to over-simplified assumptions. For example, in a real case, the convection field is unsteady over time and the concentration rarely homogeneous in the x and y directions.

3.1.2 Hassan and Eltayeb's model

Hassan and Eltayeb[18] proposed a model according to the Eulerian diffusion equation of Pasquill[17], Eq.3.1. Hassan and Eltayed made assumptions based primarily on the data from dust transport experiments in wind tunnel, and they simplified Eq.3.1 but avoided the limitation of Gillette and Goodwin's model, resulting in a model that still could be solved analytically,

$$U\frac{\partial c}{\partial x} = \frac{\partial}{\partial z}(D_z\frac{\partial c}{\partial z}) - w_t\frac{\partial c}{\partial z} \tag{3.4}$$

where U is the steady velocity along the streamline depending on the height z only ($U(z) = \beta z^m$ with β and m constants); D_z is again the diffusion coefficient in $z-$direction; w is the settling velocity. Now it is assumed that c depends on x and z. This problem is defined in the simplified computational domain given as

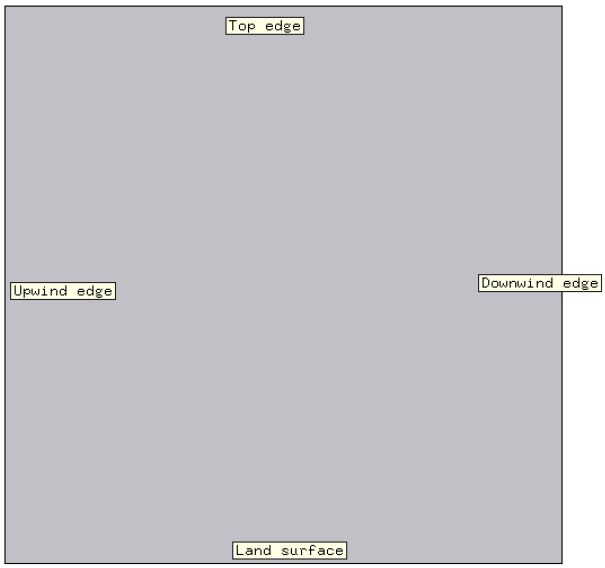

FIGURE 3.1: Computational domain for the dust model

where the bottom is the land surface; the left is upwind edge; the right is the downwind edge. In real case, the top and left edge can be infinite, but with appropriate boundary condition, we can a certain domain, well-defined. We will see that in the coming sessions, how the boundary conditions are assigned and the corresponding analytical or numerical solutions are derived from the literature.

It is true that Eq.3.4 could be solved analytically but specific boundary conditions are necessary, which help transform the Partial Differential Equation into an Ordinary Differential Equation. Hassan and Eltayeb[18, 19] specified two types of boundary conditions for which the Partial Differential Equation could be solved. The first group of boundary conditions is,

$$\begin{cases} c(0,z) = F(z) \\ c(\infty,z) = 0.0 \\ c(x,\infty) = 0.0 \end{cases} \tag{3.5}$$

These boundary conditions have specific means in real cases: the concentration near the surface has to be fixed with a function $F(z)$, and it approaches zero in far downwind and infinite heights in the atmosphere. With the previous boundary conditions, the analytical solution is similar to Eq.3.3, with a slight modification of the exponent, assuming that below z_0 there is a restriction placed on the concentration,

$$\begin{cases} c(z) = c(z_0)(\frac{z_0}{z})^{\nu} & \text{if } z \geq z_0 \\ c(z) = 0 & \text{if } z < z_0 \end{cases} \tag{3.6}$$

where define the coefficient $\nu = \frac{w_t}{\lambda(m+1)}$; λ and m are coefficients too. This solution means that the concentration profile decays away from the bottom

surface towards zero as increasing height in the atmosphere, but noting that this case represents the diffusion of a decaying concentration profile with no other addition sources or sinks.

At the end of the paper, Hassan and Eltayeb[18] mentioned that their colleagues have suggested to obtaining the solution with the following boundary conditions:

$$\begin{cases} c(0,z) = 0.0 \\ c(x,\infty) = 0.0 \\ c(x,0) = F(x) \end{cases} \tag{3.7}$$

In this case, the first condition represents that there is no upwind dust concentrations, the second condition means at infinite heights the dust is zero, and the last implies concentration on land surface is a function of streamline distance. Eltayeb and Hassan[19] solved this problem after a Laplace transform of the boundary conditions,

$$\begin{cases} c(0,Z) = 0.0 \\ c(X,\infty) = 0.0 \\ c(X,Z_0) = c_0 g(X) \end{cases} \tag{3.8}$$

where X and Z are transformed variables defined as

$$Z = z^{(m+1)/2} \quad X = \frac{\lambda(m+1)^2}{4\beta}x \tag{3.9}$$

where $g(X)$ is a boundary concentration profile function and the other variables are as defined before. A complete analytical Laplace transform is possible for $g(X) = 1$,

$$c(X,Z) = c_0(\frac{Z_0}{Z})^{2\nu}\frac{\Gamma(\nu, Z^2/4X)}{\Gamma(\nu)} \quad Z_0 \to 0 \tag{3.10}$$

where $\Gamma(\nu)$ is the Gamma function and $\Gamma(\nu, Z^2/4X)$ is the incomplete Gamma function.

3.1.3 Roney and White' model

Roney and White[20] studied the Eltayeb and Hessan's[19] model, and they found that the solution of Eltayeb and Hassan appears to be inappropriate for $PM10$ particles as the constant parameter ν defined previously in Eq.3.6 becomes very small ($\nu \approx 0.005$), giving large Γ values when evaluated in the Gamma Function $\Gamma(\nu) \approx 200$. Likewise, the Incomplete Gamma Function $\Gamma(\nu, Z^2/4X)$ is small except for when $Z = 0$, where it reverts to the Gamma function. Thus, the ratio of the Incomplete Gamma Function to the Gamma Function is always less than one for this case, except when $Z = 0$. This ratio creates a large difference between the concentrations as $z \to 0$ and $z = 0.01$.

The non-physical result thus seems to be an artifact of the Gamma Function solutions, which are highly non-linear at small values of the independent variable.

Roney and White thus proposed a solution of the form which could circumvent the small particle problem in the analytical solution[20] ,

$$c(X,Z) = c_0(\frac{Z_0}{Z})^{2\nu}\frac{\Gamma(\nu, Z^2/4X)}{\Gamma(\nu, Z_0^2/4X)} \tag{3.11}$$

where we could see that $\Gamma(\nu)$ is replace by $\Gamma(\nu, Z_0^2/4X)$ in the denominator, and also this solution requires $Z \geq Z_0$. Although the solution is no longer an exact solution to the partial differential equation, it represents a good approximation for those cases in which Z_0 and ν are small.

A brief summary, we can have the analytical solution in a $2D$ domain for the dust concentration, but this solution is limit to very specific cases. In order to have a much general solution to this problem, we are going to analyze the erosion mechanism from the very beginning, explain the concept of threshold friction velocity, horizontal saltation flux and vertical dust flux, and give the numerical solution to the mathematical model.

3.2 Threshold velocity

3.2.1 Modeling of threshold velocity

The threshold velocity, u_{*t}, is the friction velocity at which wind erosion is initiated. The value of u_{*t} for specific particles depend heavily on many factors such as soil texture, soil salt content, surface crust, roughness and the distribution of vegetation.It can be expressed as a function of particle size, but this is only for idealized soils. There are many theories to formulate u_{*t} and the the particle size, derived for uniform and spherical particles spreading loosely over a dry and bare surface[21, 22, 23]. Bagnold[21] firstly obtained a simple expression for u_{*t} taking into account the force balance between the aerodynamic drag and the gravity force, and he found that $u_{*t} \propto d^{1/2}$, where d is the diameter of the particle. Bagnold's expression works very well for particle sizes larger than $100\mu\mathrm{m}$ but fails to predict the minimum of u_{*t} when d is at around $75\mu\mathrm{m}$, and also fails to show the subsequent increase of u_{*t} with decreasing particle size. Greeley and Iversen[22] considered the cohesive force and aerodynamic lift, but not the aerodynamic drag and gravity force, and further found that

$$u_{*t} = A_B\sqrt{\sigma_p g d}F(\mathrm{Re}_{*t})\mathrm{G(d)} \tag{3.12}$$

where A_B, the dimensionless threshold friction velocity, is a coefficient depending on the Reynolds number ,$\mathrm{Re}_{*\mathrm{t}}$; F is a function of the Reynolds number for specific particle at threshold friction velocity; G is a function of the diameter d; σ_p is the particle to air density ratio; g is the gravitational acceleration. These parameters are all estimated from tunnel experiments. This new expression overcomes the drawback arising from Bagnold's expression and fits much better u_{*t} in a large range of the particle diameter d. However, the two empirical functions F and G have complex and unreasonable expressions, possibly because of a misfit of $G(d)$.

Based on previous work, Shao and Lu[24] take into account the effect of inter-particle cohesion on u_{*t} and give the following explicit expression for the threshold friction velocity,

$$u_{*t} = \sqrt{A_N(\sigma_p g d + \frac{\gamma}{\rho_p d})} \tag{3.13}$$

where A_N explicitly accounts for the effects of inter-particle cohesion with value around 0.0123; γ is a constant with value around $3 \times 10^{-4}\mathrm{kg} \cdot \mathrm{s}^{-2}$; ρ_p is the density of the particle. This new formulation is obtained for spherical particles loosely spread over a dry and bare surface. However, the real particles are not identically smooth and spherical. Other types of inter-particle forces such as capillary and Coulomb forces relying strongly on the moisture and chemical agents among particles are not accurately approximated.To account for the effects of surface roughness, soil moisture and aggregation on u_{*t}, the threshold friction velocity is corrected in the following form

$$u_{*t} = u_{*t0} R(\lambda) H(\omega) M \tag{3.14}$$

where R, H and M are the correction functions describing the influence of roughness element, soil moisture and soil surface aggregation and crusting[25]. λ is the frontal area index of the surface roughness elements(a measure of surface cover) and ω is the volumetric fractional soil moisture content on the particle surface. According to their physical means, $H(\omega)$ function satisfies $H(\omega) = 1$ when $\omega = 0$ and $H(\omega) \to \infty$ as ω becomes large. Likewise, $R(\lambda) = 1$ when $\lambda = 0$(no cover) and $R(\lambda) \to \infty$(extensive cover) when λ grows. Thus, these functions both act to increase u_{*t} as wetness or surface cover increase.

3.2.2 Correction factor for soil moisture

Soil moisture strongly affects the threshold friction velocity since it enhances soil cohesion. Fecan et al[26] attempted to parameterize the influence of soil moisture as a function of clay content through fitting the equation with the experimental data for various soils. Y. Shao and E. Jung[1] investigated Fecan's parameterization for several kinds of soil texture using observation

data and they finally expressed the correction function as

$$H(\omega) = \begin{cases} 1, & \text{for } \omega \leq \omega_r \\ \sqrt{1 + a(\omega - \omega_r)^b}, & \text{for } \omega > \omega_r \end{cases} \tag{3.15}$$

where ω is the volumetric soil moisture, a and b are constants that vary on the soil texture, and ω_r is the threshold soil moisture. Shao and Jung's coefficients fitted from experimental data for different soil types are listed in table 3.1. It is clearly shown that the effect of moisture on threshold friction velocity can vary significantly among soil types, but this could limit the application of this formulation because we usually do not know the parameters for a specific soil.

TABLE 3.1: The a, b, and ω_r values in soil moisture correction for different soil types

	Sand	Loamy Sand	Sandy Loam	Loam	Silt Loam	Sandy Clay Loam	Clay Loam	Sandy Clay	Silty Clay	Clay
a	21.19	30.0	44.87	17.79	21.79	25.79	29.86	25.20	22.90	20.47
b	0.68	0.90	0.85	0.61	0.67	0.74	0.80	0.70	0.65	0.59
ω_r	0.005	0.01	0.037	0.049	0.059	0.075	0.095	0.125	0.140	0.156

The disadvantages of previous experiment-based parameterization for moisture correction was overcome by Shao[25], who proposed another correction factor as exponential function, Eq.3.16. And later,this correction term was improved by Zhao[27] et al considering different range of moisture proportion, Eq.3.17, which is implemented in Haustein's model[28].

$$H(\omega) = \exp(22.7\omega) \tag{3.16}$$

$$H(\omega) = \begin{cases} \exp(22.7\omega), & \text{for } \omega \leq 0.03 \\ \exp(95.3 \times \omega - 2.03), & \text{otherwise} \end{cases} \tag{3.17}$$

3.2.3 Correction factor for roughness

The roughness corrector is proposed in a double drag partition by Raupach et al[29], considering the bare and vegetated surfaces independently. Actually, it introduces a roughness density concerning the frontal area covered by the non-erodible roughness elements present at the surface, given by

$$R(\lambda) = (1 - \sigma_v m_v \lambda_v)^{1/2}(1 + m_v \beta_v \lambda_v)^{1/2}(1 - \frac{\sigma_b m_b \lambda_b}{1 - f_c})^{1/2}(1 + \frac{\beta_b m_b \lambda_b}{1 - f_c})^{1/2} \tag{3.18}$$

where β is the ratio of the drag coefficient for a single roughness element to that of the surface without roughness element; σ is the ratio of basal to frontal area of the roughness elements; m, varying between 0 and 1, accounts for the spatiotemporal variations of the stress of the underlying surface. They are obtained for barren and vegetated surfaces separately. The suggested parameter values are that $\beta_v = 202$, $m_v = 0.16$ and $\sigma_v = 1.45$, $\beta_b = 90$, $m_b = 0.5$ and $\sigma_b = 1$. f_v is the vegetated cover fraction(default =0 in our case, meaning there is no vegetation). The roughness density, λ, is also calculated differently for barren (λ_b) and vegetated surfaces (λ_v). These parameters vary significantly with surface types and the spatial distribution of roughness elements. In the presence of vegetation, a straightforward parameterization for λ_v is proposed by Shao et al[25] is

$$\lambda_v = -c_\lambda \ln(1 - f_v) \tag{3.19}$$

where c_λ is a coefficient accounting for the distribution and orientation of the roughness element. The suggested value of c_λ is 0.35, which is suitable for stubble roughness. On the other hand, the roughness density on bare surface arising from solid elements can be related to the geometrical fractional area (f_c) of the solid elements and of their shape factor (η). In a real application , it is nearly impossible to derive the mathematical relation among these parameters, so only anecdotal data for λ_b are available from the literature[30, 28]. One possibility is to construct a database with general roughness densities for bare sandy and gobi surfaces based on the measurement of Marticorena[31] and relate them to the current model. Usually, suggested λ_b is 0.002 for sandy desert and 0.15 for gobi desert. A satisfactory expression for M is not available at this stage and hence the values of M are temporarily set to 1 for all soils[2].

Field observations have shown that increasing surface cover, or roughness, is an effective technique to prevent wind erosion[32]. Non-erodible roughness elements absorb part of the momentum transferred from the atmosphere to the surface and reduce the shear force on mobile particles. These roughness elements can either be vegetation(living or dead) or nonerodible soil fractions(usually defined as dry aggregates with diameter $\geq 0.85\mathrm{mm}$). Two commonly used measures of are the vegetated cover fraction f_v(viewed from the above) and the bare roughness density λ_b.

3.3 Flux

One challenge in dust modeling is to predict the emission rate of particles in all size groups. For this purpose, many efforts have been made to develop physically sound yet simple schemes of dust emission rate.The main mechanism for dust emission is widely considered to be aggregate disintegration and saltation bombardment. Based on this kind of emission mechanism, the dust emission rate, the quality of the dust moving upward across the level

near the surface per unit time and unit area, is measured by an equivalent physical quantity, given by

$$F(d_i, d_s) = \alpha(d_i, d_s)Q(d_i, d_s) \tag{3.20}$$

where F is vertical dust emission flux for the ith particle group of size d_i generated by the saltation of particles of size d_s, α is a coefficient depending both on d_i and d_s, Q is the horizontal saltation flux denoted as vertical integral of the streamwise saltating particle flux density with unit $\mathrm{kg} \cdot \mathrm{m}^{-1} \cdot \mathrm{t}^{-1}$. Wind tunnel experiments give empirical expressions, showing that the order of magnitude of α is $10^{-5}\mathrm{m}^{-1}$[25, 33]. The α coefficient considers the impact of kinetic energy of saltation particles and the binding energy, ψ, of dust particles which are two quantities key to dust emission[34]. Unfortunately, ψ is difficult to measure, which motivates us to find other parameterization.

3.3.1 Horizontal saltation flux

The horizontal saltation flux usually indicates the intensity of saltation. Models to estimate particulate matter emissions from windblown dust are generally based on the local wind speed, the threshold wind speed to initiate erosion, and the soil texture of a given surface. However, precipitation, soil crusting, and soil disturbance and dramatically change the threshold wind speed and erosion potential of a surface, making modeling difficult[35]. Here we could simply give the following parameterization for the horizontal saltation flux.

1. Kawamura[36]
   Kawamura was the first to explicitly introduce the threshold shear velocity term, u_{*t}, into his transport model, which also used physical arguments:
   $$Q = C_{kw}\frac{\rho_{air}}{g}(u_* - u_{*t})(u_* + u_{*t})^2 \tag{3.21}$$
   where his original empirical constant of proportionality is $C_{kw} = 2.78$. Horikawa[37] , based upon field data from experiments, suggested C_{kw} is closer to 1.0. White[38] found $C_{kw} = 2.61$ fits much better for aeolian transport on the mars in his evaluation of the applicability of Kawamura's model.

2. Owen(1964)[39]
   Owen developed his model based upon arguments concerning the concentration and vertical distribution of saltating particles on the surface. The horizontal sand flux has the following form,
   $$Q = \frac{\rho_{air}}{g}u_*^3(1 - \frac{u_{*t}^2}{u_*^2})(C_{o1} + C_{o2}\frac{w_s}{u_*}) \tag{3.22}$$

where C_{o1} and C_{o2} have values of 0.25 and 0.33, respectively, and w_s is the particle fall velocity, which could be computed according to the formulation developed by Chen[40].

3. Sorensen(2004)[41]
   Sorensen developed an analytical model that incorporates physics similar to those of the preceding models and accounts for particle saltation rates and estimates of air-borne(and thus particle-borne) shear stress, following Owen[39], so that:

$$Q = \frac{\rho_{air}}{g} u_*^3 (1 - (\frac{u_{*t}}{u_*})^2)[C_{s1} + C_{s2}(\frac{u_{*t}}{u_*})^2 + C_{s3}\frac{u_{*t}}{u_*}] \tag{3.23}$$

   However, the constants (like C_{s1}, C_{s2} and C_{s3}) in this equation are sensitive to particle size. Only a limit group of parameters is given according to the wind tunnel experiment at different size of particle diameters[41], so the drawback of this parameterization is obvious, we are unable to expand it to any particle diameters.

4. Marticorena and Bergametti's scheme[42].
   The horizontal sand flux can be calculated using the saltation formulation proposed by White

$$Q = C_{MB} \cdot \frac{\rho_{air}}{g} \cdot u_*^3 \cdot (1 + \frac{u_{*t}}{u_*}) \cdot (1 - \frac{u_{*t}}{u_*^2}) \tag{3.24}$$

   where the correction factor C_{MB} which was used to adjust the saltation flux according to experimental results was originally set to 2.61 following the experimental results of White[38] but later revised to 1.0[43, 44].

5. Shao's scheme
   Shao proposed the sand transport formulation based on Owen' model with finally a dimensionless constant C_{Shao} that could vary from 1.8 to 3.1 but this constant is usually set to 2.45[45],

$$Q = C_{Shao} \cdot \frac{\rho_{air} \cdot u_*^3}{g} \cdot (1 - \frac{u_{*t}}{u_*}) \tag{3.25}$$

3.3.2 Vertical dust flux

The vertical dust flux F is defined as the emitted dust mass concentration per unit area per unit time($\mathrm{kg \cdot m^{-2} \cdot t^{-1}}$). It can be parameterized in terms of the fact that vertical dust flux is related to horizontal sand flux. Numerous attempts have been made to parameterize vertical dust flux through an empirical method using data fitting or through a physically based method, by considering balance of the volume saltated during dust emission process. There are mainly two group of vertical dust flux expressions proposed by different research groups. Here we will introduce both of them.

1. Marticorena and Bergametti's(MB) scheme[42].
   In the MB scheme, the vertical and horizontal flux is related to the clay content. Marticorena and Bergametti showed that when plotting the mean ratio of total vertical flux to total horizontal flux with respect to the clay content, there is a clear trend for soils that have clay less than 20%, and they proposed a linear fitting equation,

$$F = 100 \times Q \times 10^{(0.134 \times C_c - 6.0)}, \quad C_c \leq 20\% \tag{3.26}$$

   where C_c is the presence of the clay content. Despite simplicity, the weakness of the MB scheme is that its parameterization is not applicable to soils that have more than 20% clay and other kind of soils, and the physical processes are not involved in this parameterization.

2. Lu and Shao's scheme[46].
   According to Lu and Shao's research, the dust emission rate is determined based on the volume of removal caused by saltating particles when they strike the surface. By modeling the ploughing process of individual saltating particles with the assumption of an impact angle of a saltating particle,assuming the striking angle $\alpha = 13^\circ$, a simplified total vertical dust flux equation can be expressed as

$$F = \frac{C_\alpha g f \rho_b}{2p}(0.24 + C_\beta u_* \sqrt{\frac{\rho_p}{p}})Q \tag{3.27}$$

   where p is the plastic pressure of the soil surface with unit Pa, which means surface hardness, f is the fraction of dust contained in the volume, ρ_b and ρ_p are the bulk-soil and soil particle density, respectively, and ρ_p/ρ_b is around 2.6. C_α and C_β are constant, given by the following range,

$$C_\alpha \in [0.0002, 0.001]$$
$$C_\beta \in [0.63, 2.09]$$

3. Shao's 2004 Scheme[47].
   Shao further proposed a new dust emission parameterization which considers mainly two kind of dust emission mechanisms: aggregate disintegration and saltation bombardment. The dust emissions from saltation bombardment can be estimated by modeling the removed volume as in previous conclusion from Lu and Shao[46], and the aggregate disintegration was newly parameterized[47] with the assumption that aggregates disintegrate only when they strike the surface. By supposing that particles are divided into continuous I particle-size intervals, he proposed a size-resolved dust emission. Shao[48] finally simplified this approach and expressed this dust emission flux for particles of size d_i by saltation of particles of size d_s as

$$F(d_i, d_s) = c_Y \eta_f [(1-\gamma) + \gamma\sigma_p](1+\sigma_m)\frac{g}{u_*^2}Q \tag{3.28}$$

where c_Y is a dimensionless coefficient, η_f is the mass fraction of the dust particles having diameter less than $20\mu\mathrm{m}$ contained in a unit of soil mass, and the other notations are as described earlier(hereinafter denoted as the S04 scheme).

For given soil texture and friction velocity, the model only requires the estimate of σ_m to compute F.Lu and Shao[46] derived an expression for the volume removed by an impacting saltation particle, Ω. if the particle impact angle is set to $15°$, we have

$$\Omega = \frac{U^2 d_s}{\beta^2}(0.24 + 0.21U\sqrt{\frac{\rho_p}{p}}) \tag{3.29}$$

where $\beta = \sqrt{2pd_s/m}$ and p is the soil plastic pressure; m is the saltating particle mass; ρ_p is the particle density; U is the particle impact velocity and the impact angle is set to $\alpha = 15°$. Since $m_\Omega = \rho_b\Omega$ with ρ_b being the soil density, U is around $10u_*$ and ρ_p/ρ_b is around 2.6 (assuming $\rho_p = 2600\mathrm{kg}\cdot\mathrm{m}^{-3}$ and $\rho_b = 1000\mathrm{kg}\cdot\mathrm{m}^{-3}$), we obtain[48]

$$\sigma_m = 12u_*^2\frac{\rho_b}{p}(1 + 14u_*\sqrt{\frac{\rho_b}{p}}) \tag{3.30}$$

$$\eta_f \in [3.2\%, 72\%] \tag{3.31}$$

$$\gamma = \exp[-(u_* - u_{*t})^3] \tag{3.32}$$

$$\sigma_p = \frac{p_m(d_i)}{p_f(d_i)} \tag{3.33}$$

TABLE 3.2: Dimensionless coefficient c_Y and plastic pressure p for different soil types

	Sand	Loam	Sandy Clay Loam	Silty clay loam	Clay
Plastic pressure(Pa)	5000	10000	10000	30000	50000
c_Y	5×10^{-5}	3×10^{-5}	5×10^{-5}	1×10^{-5}	1×10^{-5}

3.4 Mathematical model

3.4.1 Coupled model

We propose in the following a model coupling the transient-convection-diffusion equation and the Navier-Stokes equations.

Small and neutrally buoyant particles exactly have the same velocity to fluid flow, and thus their dynamic behavior can be described by the unsteady convection diffusion reaction equation mainly with convection velocity $\boldsymbol{v}$ and diffusion, D. However, some particles whose density is different to that of the fluid, either larger (e.g. mineral grains, sand storms) or smaller (e.g. gas bubbles) will have an additional vertical velocity, w_t, constituting another part in the convection. This vertical velocity is called settling velocity here, which is proportional to the density difference between the fluids and particles and to the particle geometry diameter, d.

$$\begin{cases} c_t + \boldsymbol{a} \cdot \nabla c - \nabla \cdot (D \nabla c) + sc = f \\ c = c_D \text{ on } \Gamma_D \\ \boldsymbol{n} \cdot (D \nabla c) = F \text{ on } \Gamma_N \end{cases} \tag{3.34}$$

$$\begin{cases} \boldsymbol{v}_t + \boldsymbol{v} \cdot \boldsymbol{\nabla} \boldsymbol{v} - \nabla \cdot (\nu \nabla \boldsymbol{v}) + \nabla p = \boldsymbol{b} \text{ in } \Omega \\ \nabla \cdot \boldsymbol{v} = 0 \text{ in } \Omega \\ \boldsymbol{v} = \boldsymbol{v}_D \text{ on } \Gamma_D \\ -p\boldsymbol{n} + \nu(\boldsymbol{n} \cdot \nabla)\boldsymbol{v} = \boldsymbol{t} \text{ on } \Gamma_N \\ \boldsymbol{v}(\boldsymbol{x}, 0) = \boldsymbol{v}_0(\boldsymbol{x}) \end{cases} \tag{3.35}$$

where the vector $\boldsymbol{n}$ denotes the unit outer normal to the boundary; F is the vertical dust flux which has been analyzed in the previous section; s is the reaction coefficient; f is the source term; $\boldsymbol{a}$ is the convection velocity including fluid velocity and settling velocity, which we shall discuss more about this in the next session. We could understand the physical phenomenon in the following way: In a given region, assuming the particles have similar size and density, the concentration on some boundaries have already been known (Dirichlet boundary conditions on Γ_D), and in some boundaries(Neumann boundary conditions on Γ_N) such as the surface ground, the particles are generated by the erosion process due to the fluid motion. Inside this region, particles are convected with an advection velocity $\boldsymbol{a}$ and diffusion exists also due to the gradient of the particle concentration. If there are no source and no reaction in the problem, f and s can be 0.

On the other hand, the flow problem is given in Eq.3.35, where the vector $\boldsymbol{n}$ again denotes the unit outer normal to the boundary; $\boldsymbol{v}$ is the flow velocity; $\boldsymbol{b}$ is the body force of the flow; $\boldsymbol{v}_D$ is the given velocity on the Dirichlet boundary; $\boldsymbol{v}_0$ is the initial status of the flow; ν is the kinematic viscosity and p the kinematic pressure. It is also necessary to note that $\boldsymbol{v}$, $\boldsymbol{v}_D$, $\boldsymbol{v}_0$ and $\boldsymbol{b}$ are in vector form and ν is second-order tensor. The original Navier-Stokes equations can be used to describe the motion of both compressible and incompressible flow. In our case, we choose the incompressible Navier-Stokes equations which fit well for the current problem because in a natural region, it is rare to have the flow (e.g. wind or water) whose Mach number is larger than 0.3.

Up to now, we have the coupled model for our physical problem. The coupling is that the flow velocity is the condition for initiating the dust once the friction velocity is large enough. Then the dust particle is convected by integrated the flow velocity and the dust settling velocity, which we will see in the next section. Considering the techniques required to solve coupled problems, we have two main kind of schemes. One is the monolithic or simultaneous scheme, in which we solve the equations associated to all the problems in a single system,simultaneously. However, the monolithic approach sometimes has some disadvantages: a) the system of equations to be solved could result in extremely large matrix after integrating all the equations; b) The system of equations to be solved can be ill-conditioned because it involves different physical problems with different constitutive equation laws and physical parameters; c) modularity is difficult to obtain since we cannot couple independent pieces of software and assemble each problem into a global matrix.

Another option is to take each of the problems to be solved independently. The interaction with the other problems is treated as an external given term which is iteratively communicated between the coupled systems. Advantages for such scheme are as follows: a) customization, each field can be treated with algorithms which are known to perform well for the isolated problem; b) independent modeling, partitioned schemes facilitate the use of of non-matching meshes (once used) ; c) software reuse, independent pieces of software can be used to deal with each of the problems; d) modularity, each physical problem can be packed in a software module, all implementations for the particular problem are localized in its module. So we will explain our finite element method to solve the equations independently based on the idea of partitioned schemes in coming sessions.

3.4.2 Particle settling

Motion of the fluid could transport particles which are either more dense (e.g. sand storm, mineral sediment) or less dense (e.g. bubbles) than the fluid. Intuitively we regard the convection velocity $\boldsymbol{a}$ in Eq.3.34 is the same as the flow velocity $\boldsymbol{v}$, but this is not the fact. It is necessary to introduce the settling velocity $\boldsymbol{w}_t$ arising from the gravitational effect.

In order to estimate the expression for the settling velocity, we consider the conservation of momentum in the vertical direction with three kind of acting forces, i.e., weight, buoyancy and drag. With the assumptions given in previous sections about the shape of the particle, we here again consider the particle as solids with spherical diameter d and density ρ_p. The fluid density is ρ_a. In a 3-D coordinate system with z being the negative gravity direction $(-\boldsymbol{e}_z)$, we have

$$\text{Weight} = -\rho_p g \frac{\pi}{6} d^3 \boldsymbol{e}_z$$

$$\text{Buoyancy} = \rho_a g \frac{\pi}{6} d^3 \boldsymbol{e}_z$$

$$\text{Drag} = -\frac{1}{2}\rho_a C_d \frac{\pi d^2}{4} \boldsymbol{w}_t ||\boldsymbol{w}_t||$$

C_d is the drag coefficient for the sphere and is predicted as a function of the Reynolds number, i.e. $\mathrm{Re} = \frac{\mathrm{w_t d}}{\nu}$, the conservation of vertical momentum is,

$$\frac{\pi}{6}\rho_p d^3 \frac{\partial \boldsymbol{w}_t}{\partial t} = \frac{\pi}{6}(\rho_a - \rho_p) g d^3 \boldsymbol{e}_z - \frac{\pi}{8}\rho_a C_d d^2 \boldsymbol{w}_t ||\boldsymbol{w}_t|| \tag{3.36}$$

From now on, we shall consider how to solve Eq.3.36 for $\boldsymbol{w}_t = [0, 0, w_t]^T$. Let us consider following reasoning: suppose that a particle is originally at rest ($\boldsymbol{w}_t = 0$). If $\rho_p > \rho_a$, the particle will start to accelerate downward ($\partial \boldsymbol{w}_t / \partial t < 0$). When the value of w_t increases, the corresponding drag forces increases too but acts in an opposite direction. Eventually the drag force is large enough to balance the weight force and buoyancy force, making the acceleration, $\partial \boldsymbol{w}_t / \partial t < 0$, equals to 0 and $\boldsymbol{w}_t$ becomes constant. The finally constant value of $\boldsymbol{w}_t$ is called terminal velocity. Typically the time required to reach this constant velocity is very short compared with the time scale we are analyzing. So we can solve Eq.3.36 for $\boldsymbol{w}_t$ by setting $\partial \boldsymbol{w}_t / \partial t = \mathbf{0}$, and the terminal velocity can be estimated as a function of particle size, given as

$$w_t = -\sqrt{\frac{4(\rho_p - \rho_a) g d}{3 \rho_a C_d}} \tag{3.37}$$

where C_d is the drag coefficient predicted as a empirical function of the Reynolds number, $\mathrm{Re} = \frac{\mathrm{w_t d}}{\nu}$

$$C_d = \begin{cases} \frac{24}{\mathrm{Re}} + \frac{3}{\sqrt{\mathrm{Re}}} + 0.34 & \text{if } \mathrm{Re} < 1 \times 10^4 \\ \frac{24}{\mathrm{Re}} & \text{if } \mathrm{Re} < 1 \text{ creeping flow} \end{cases} \tag{3.38}$$

From Eq.3.37 and Eq.3.38, we could find that the strategy to compute the particle settling velocity unavoidably requires to solve a non-linear equation. This can be done through the fixed point method and iterated until given accuracy is reached. After we have the settling velocity is known, the final version of the convection velocity is

$$\boldsymbol{a} = \begin{bmatrix} v_1 \\ v_2 \\ v_3 \end{bmatrix} + \begin{bmatrix} 0 \\ 0 \\ w_t \end{bmatrix}$$

where $(v_1, v_2, v_3)^T$ is the component of the flow velocity $\boldsymbol{v}$.

3.4.3 Particle diffusion

If the fluid flow is in a low Reynolds number, the diffusion of particles could be estimated through the diffusion of dissolved particles which heavily depend on the Brownian motion of the fluid molecules. Based on the random walk model in which the motion and kinetics of the suspended particles result from the impact by the fluid molecule, the diffusion coefficient , D, is given by the Stokes-Einstein equation[49],

$$D = \frac{kT}{6\pi\mu r} \tag{3.39}$$

where T is the absolute temperature; k is the Boltzmann constant, $k = 1.381 \times 10^{-23}\mathrm{J/K}$; r is the radius of the particle; μ is the dynamic viscosity, $\mu = \nu \times \rho_a$.

In turbulent flow with a relatively large Reynolds number, the velocity is sufficiently rapid to maintain a uniform particle quantity, keeping the suspension of particles, although there are still some particles losing due to settling effect on the boundary. We could, for simplification, assume the diffusion coefficients for particles in this case to be the same as those dissolved particles in low Reynolds number, which would not affect our model too much.

Chapter 4

Numerical approximation

In this chapter we are trying to solve the PDEs we proposed to model the dust dynamics in the atmosphere. The Galerking finite element method is used for spatial discretization of the PDEs, while finite difference methods is used for temporal discretization. However, in case of convection dominated case, stabilization methods like variational multi-scale, GLS and SGS are required in order to eliminate the oscillations. These stabilized finite element formulations yield a globally stable solution but it is still possible that in some regions the concentration has very large gradient, local instabilities may appear and pollute the solution; the so-called shock capturing method is introduced in our problem.

4.1 Trial solution and weighting functions

In order to obtain the weak, or variational, form of Eq.3.34 and Eq.3.35, it is necessary to define two classes of functions: the *test* functions and the *trial* solutions. Functional spaces are introduced based on the standard Galerkin finite element discretization.

Let $L^2(\Omega)$ be the space of square integrable functions in the domain. The first class of functions, denoted by $\mathcal{V}$, including *test* functions and all functions which are square integrable, have square integrable first derivatives over the whole computational domain Ω^d(superscript d meaning the number of dimension), and vanish on the Dirichlet boundary, Γ_D. $\mathcal{V}$ is defined,

$$\mathcal{V} = \{\omega \in \mathcal{H}(\Omega) | \omega = 0 \text{ on } \Gamma_D\} \tag{4.1}$$

where $\mathcal{H}$ is a Sobolev space, defined according to $\mathcal{L}^2(\Omega)$ the space of functions which are square integrable over the computational domain Ω,

$$\mathcal{H}(\Omega) = \{v \in \mathcal{L}^2(\Omega) | \frac{\partial v}{\partial x_i} \in \mathcal{L}^2(\Omega) \quad i = 1, \cdots n_d\}$$

where n_d is the number of dimension.
Another set of functions is the *trial solution* space, denoted by $\mathcal{S}$. This set

of functions are definite similar to the test functions except that they are required to satisfy the Dirichlet conditions on Γ_D:

$$\mathcal{S} = \{u \in \mathcal{H}(\Omega) | u = u_D \text{ on } \Gamma_D\} \equiv \mathcal{V} + \{\bar{u}_D\} \tag{4.2}$$

where $\bar{u}_D$ is any function in $\mathcal{H}(\Omega)$ fulfilling the Dirichlet boundary, i.e. such that $u_D = \bar{u}_D$ on Γ_D. So $\mathcal{S}$ can be regarded as of a translation of $\mathcal{V}$ and is thus the so-called affine space. In case of homogenous boundary conditions, $u_D = 0$, trial and test spaces coincide, $\mathcal{V} = \mathcal{S}$.

Finally, we have to define the space of function, $\mathcal{Q}$, for the pressure, which are required to be square-integrable. Because the collections $\mathcal{V}$, $\mathcal{S}$ and $\mathcal{Q}$ involve infinite number of functions, in the finite element method, they are approximated by a finite-dimensional subsets obtained by replacing themselves with finite dimensional subspaces, denoted by $\mathcal{V}^h$, $\mathcal{S}^h$ and $\mathcal{Q}^h$ respectively. These subspace functions are defined through low-degree polynomials on small elements discretized from the original computational domain Ω.

4.2 Discretization of TCDR equation

In order to explain the numerical procedure to solve the TCDR equation, we introduce some notation. The symbol $< \cdot, \cdot >$ means the integral of product of two functions, including the duality pairing, and $(\cdot, \cdot)$ denotes the $L^2(\Omega)$ inner product. The variational form of the problem in Eq3.34 can be deduced through multiplying by a test function $v \in \mathcal{V}$,

$$(v, \frac{\partial c}{\partial t}) + < v, \mathcal{L}(c) > = < v, f > \quad \forall v \in \mathcal{V} \tag{4.3}$$

and integration by parts, the variational problem becomes: find $c \in \mathcal{S}$ such that

$$(v, \frac{\partial c}{\partial t}) + B(c, v) = < v, f > + (v, F)_{\Gamma_N} \quad \forall v \in \mathcal{V} \tag{4.4}$$

with the operator

$$\mathcal{L}(c) = \boldsymbol{a} \cdot \nabla c - \nabla \cdot (D \nabla c) + sc$$

$$B(c, v) = (D \nabla c, \nabla v) + (\boldsymbol{a} \cdot \nabla c, v) + s(c, v)$$

and with approximate boundary conditions and initial conditions.

4.2.1 The Galerkin finite element discretization

The finite element approximation for the continuous variational problem in Eq.4.4 can be done with the standard Galerkin method. Let us consider a finite element partition $\{\Omega^e\}_{e=1}^{n_{el}}$ of the original computational domain Ω,

where h is the characteristic diameter for the partitioned elemental domain Ω^e. Denote $\mathcal{S}_h$ the associated finite element space to approximate $\mathcal{S}$ and the test function space $\mathcal{V}_h$ including finite dimensional piecewise polynomial space.The discretized variational problem becomes,

$$(v_h, \frac{\partial c_h}{\partial t}) + B(c_h, v_h) =< v_h, f > +(v_h, F)_{\Gamma_N} \quad \forall v_h \in \mathcal{V}_h \tag{4.5}$$

again together with approximate initial conditions and boundary conditions. However, when this Galerkin method is applied to the case in which D is small, nodal oscillations may appear due to the lack of diffusion in discretized formulation in a convection dominant case.

4.2.2 Temporal discretization

Finite difference schemes are the most common method for time discretization, for example, the θ-family method,Runge-Kutta methods and Padé approximation. Here for simplification,we adopt the θ-family methods which is widely used for integrating 1st-order differential equations. This is a single step method,meaning the solution c_h^{n+1} of the problem at time $t^{n+1} = t^n + \Delta t$ is determined by that at time t^n:

$$\frac{c_h^{n+1} - c_h^n}{\triangle t} = \theta \frac{\partial c_h^{n+1}}{\partial t} + (1-\theta)\frac{\partial c_h^n}{\partial t} + \mathcal{O}((1/2-\theta)\triangle t, \triangle t^2)$$

neglecting the truncation errors,

$$\frac{\triangle c_h}{\triangle t} - \theta \frac{\partial \triangle c_h}{\partial t} = \frac{\partial c_h^n}{\partial t} \quad \text{where} \quad \triangle c_h = c_h^{n+1} - c_h^n \tag{4.6}$$

Replacing $\frac{\partial c_h}{\partial t}$ in equation 4.4, the temporal-discretized scheme is

$$\begin{aligned}(v_h, \frac{\triangle c_h}{\triangle t}) + \theta B(\triangle c_h, v_h) = -B(c_h^n, v_h) + < v_h, \theta f^{n+1} + (1-\theta) f^n > \\ +(v_h, \theta F^{n+1} + (1-\theta)F^n)_{\Gamma_N} \quad \forall v_h \in \mathcal{V}_h\end{aligned} \tag{4.7}$$

In explicit form,

$$\begin{aligned}\theta B(c_h^{n+1}, v_h) + \underbrace{(v_h, \frac{1}{\triangle t} c_h^{n+1})}_{\text{added reaction term}} =< v_h, \theta f^{n+1} + (1-\theta) f^n > -(1-\theta)B(c_h^n, v_h) \\ +(v_h, \frac{1}{\triangle t} c_h^n) + (v_h, \theta F^{n+1} + (1-\theta)F^n)_{\Gamma_N} \quad \forall v_h \in \mathcal{V}_h\end{aligned} \tag{4.8}$$

After temporal discretization, we reinterpret the TCDR equation as steady convection-diffusion-reaction equation.The only difference is that the reaction coefficient is modified considering the temporal discretization. In this case, we get the advantages that most stabilization methods for solving steady problem could be adopted here. Several methods could be derived from different values of the θ parameter.The solution is conditionally stable if $\theta < 1/2$. On the other hand, the solution is unconditionally stable if $\theta \geq 1/2$, for example, Backward Euler: $\theta = 1$, Galerkin: $\theta = 2/3$, and Crank-Nicolson: $\theta = 1/2$ are the most usual ones. Among these methods, Crank-Nicolson is the only method with second-order accuracy.

4.3 Stabilization techniques for TCDR equation

Previous discretization procedures provide very good approximation to the original TCDR equation, Eq.3.34 when diffusion is relatively large. However, the temporal discretization formulation Eq.4.7 does not consider the stabilization technique. Here the general explanation of stabilized technique is briefly described.

Classical methods which could stabilize the convective term in a consistent manner are summarized in Ref.[50] including the Streamline-upwind/Galerkin method[51], the Galerkin least-squares method[52], and the Subgrid scale method [53, 54]. These methods ensure that the solution of the differential equation and the weak form have the same solution. In fact, all these stabilized methods can be discussed in a consistent manner by adding the following term to the L.H.S. of the weak form of Eq.4.7:

$$r(c_h, v_h) = \sum_{e=1}^{n_{element}} \int_{\Omega^e} \mathcal{P}(v_h)\tau_{c_h}\mathcal{R}(\triangle c_h)d\Omega \tag{4.9}$$

where $R(\triangle c_h)$ is the residual, defined as

$$\mathcal{R}(\triangle c_h) := \frac{\triangle c_h}{\triangle t} - \theta\frac{\partial \triangle c_h}{\partial t} - \frac{\partial c_h^n}{\partial t} \tag{4.10}$$

and τ_c is the stabilization parameter (also called intrinsic time) with dimension of time; $\mathcal{P}(v_h)$ is a certain operator applied to the test function; $\mathcal{R}(\triangle c_h)$ is the residual of the differential equation. So the consistently stabilized weak form of the temporal discretized version is,

$$\begin{aligned}(v_h, \frac{\triangle c_h}{\triangle t}) + \theta B(\triangle c_h, v_h) + \underbrace{\sum_{e=1}^{n_{element}} (\tau_{c_h}\mathcal{P}(v_h), \mathcal{R}(\triangle c_h))}_{\text{Stabilization term}} = -B(c_h^n, v_h) \\ + < v_h, \theta f^{n+1} + (1-\theta)f^n > + (v_h, \theta F^{n+1} + (1-\theta)F^n)_{\Gamma_N} \quad \forall v_h \in \mathcal{V}_h\end{aligned} \tag{4.11}$$

We see that in Eq.4.11, the stabilization term is added to the Galerkin weak form. In case of a convection dominated problem in which the non-dimensional Péclet number ($Pe = \frac{|\boldsymbol{a}|h}{2D}$) could be very large, but with the implementation of stabilization technique, a globally stable solution is possible.

4.3.1 The Streamline Upwind Petrov Galerkin method

The original SUPG method was designed for solving the steady convection-diffusion equation as a method to eliminate nodal oscillations when the problem is convection-dominated and discretized by the classical Galerkin approximation. It has been known that these oscillations could be avoided by adding more numerical diffusion using the centered finite difference methods. The idea of the first Streamline-Upwind method was formulated by adding an artificial diffusion to stabilize the problem but this method could not provide a consistent formulation and also introduces too much crosswind diffusion. So the SUPG method was designed based on this idea, yielding better results and introducing less crosswind diffusion, which enables SUPG method to become a popular method, being widely used up to now.

The SUPG stabilization consists in taking the perturbation operator $\mathcal{P}$ as

$$\mathcal{P}(v_h) := (\boldsymbol{a} \cdot \nabla) v_h \tag{4.12}$$

The weak form for the SUPG method can be obtained after substitution of the perturbation operator $\mathcal{P}(v_h)$ from Eq.4.12 to Eq.4.11. It remains here to define the stabilization parameter which is another important part in the SUPG method. We could take the stabilization parameter as,

$$\tau_{c_h} = \frac{\alpha h}{2||\boldsymbol{a}||} \tag{4.13}$$

where

$$\alpha(Pe) = \coth(Pe) - \frac{1}{Pe}$$

4.3.2 The Galerkin Least Square method

In the GLS method, the previous temporal discretization analysis is usually a necessary procedure. This GLS stabilization introduces the perturbation operator $\mathcal{P}$ in strong form which is affected by the temporal discretization as follows,

$$\mathcal{P}(v_h) := \frac{v_h}{\theta \triangle t} + \mathcal{L}(v_h) = \underbrace{\boldsymbol{a} \cdot \nabla v_h}_{SUPG} + \underbrace{(s + \frac{1}{\theta \triangle t}) v_h}_{Galerkin} - \underbrace{\nabla \cdot (D \nabla v_h)}_{\text{0 in linear elements}} \tag{4.14}$$

From the practical point of view, there is no major difference between the SUPG and the GLS methods. We can see from Eq.4.14 that the first term is the SUPG weighting,the last term is zero if linear elements are used. With these terms added, the instabilities arising from the Galerkin discretization are slightly amplified in GLS compared to SUPG, but this problem could be overcome in by the simplest SGS method which will be discussed in the next session.

4.3.3 The variational multi-scale stabilization

Hughes[53] first introduced the subgrid scale method,which is widely used. One of the idea that led to the SGS method is probably due to Douglas and Wang[55] for solving the Stokes problem, where they used an equal velocity-pressure interpolation space with a stabilized finite element method similar to the GLS method. The only difference is that the SGS method proposed takes the minus of the adjoint of the operator in GLS method. The basic idea of the general method is to decompose the unknown c into a component $c_h \in \mathcal{S}_h$ which can be resolved by the finite element space and the remainder that is called the subgrid scale(SGS) component $\tilde{c} \in \tilde{\mathcal{S}}$ which is required to be approximated by a particular numerical formulation. The solution spaces $\mathcal{S}_h$ and $\tilde{\mathcal{S}}$ are such that $\mathcal{S} = \mathcal{S}_h \oplus \tilde{\mathcal{S}}$. Consistently, the approximation spaces are such that $\mathcal{V} = \mathcal{V}_h \oplus \tilde{\mathcal{V}}$.

The variational problem could be split as,

$$(v_h, \frac{\partial c_h}{\partial t} + \frac{\partial \tilde{c}}{\partial t}) + B(c_h, v_h) + B(\tilde{c}, v_h) =< v_h, f > +(v_h, F)_{\Gamma_N} \quad \forall v_h \in \mathcal{V}_h \tag{4.15}$$

$$(\tilde{v}, \frac{\partial c_h}{\partial t} + \frac{\partial \tilde{c}}{\partial t}) + B(c_h, \tilde{v}) + B(\tilde{c}, \tilde{v}) =< \tilde{v}, f > +(\tilde{v}, F)_{\Gamma_N} \quad \forall \tilde{v} \in \tilde{\mathcal{V}} \tag{4.16}$$

At this stage the objective is to approximate the subgrid scale solution in order to end up with a problem that could be solved with the finite element scale independently. After integration by parts for Eq.4.15 we shall obtain,

$$(v_h, \frac{\partial c_h}{\partial t} + \frac{\partial \tilde{c}}{\partial t}) + B(c_h, v_h) + < \tilde{c}, L^*(v_h) >=< v_h, f > +(v_h, F)_{\Gamma_N} \quad \forall v_h \in \mathcal{V}_h \tag{4.17}$$

$$(\tilde{v}, \frac{\partial c_h}{\partial t} + \frac{\partial \tilde{c}}{\partial t}) + < L(c_h), \tilde{v} > + < L(\tilde{c}), \tilde{v} >=< \tilde{v}, f > \quad \forall \tilde{v} \in \tilde{\mathcal{V}} \tag{4.18}$$

Here we adopt the adjoint operator $L^*(\cdot)$ of the operator $\mathcal{L}(\cdot)$. Formally, the adjoint operator is defined as $< v, \mathcal{L}(c) >=< c, L^*(v) >$. The duality property might involve the inter-element jump terms when finite element functions

are considered, so we assume that the sub-scale solution vanishes at the element boundaries,i.e.,

$$< \tilde{c}, L^*(v_h) > \approx \sum_{e=1}^{n_{element}} (\tilde{c}, L^*(v_h)) \equiv (\tilde{c}, L^*(v_h))_h \tag{4.19}$$

$$< \tilde{v}, L(c_h) > \approx \sum_{e=1}^{n_{element}} (\tilde{v}, \mathcal{L}(c_h)) \equiv (\tilde{v}, \mathcal{L}(c_h))_h \tag{4.20}$$

These approximations imply that jumps of derivatives of finite elements functions on element edges are neglected.

Another assumption which is the most important part, is to approximate the sub-scales since they cannot be represented by the finite element mesh. So we again introduce a stabilization parameter τ_{c_h}, such that,

$$< \tilde{v}, \mathcal{L}(\tilde{c}) > \approx \tau_{c_h}^{-1}(\tilde{v}, \tilde{c}) \text{ with } \tau_{c_h}^{-1} = c_1 \frac{D}{h^2} + c_2 \frac{|\boldsymbol{a}|}{h} + c_3 s \tag{4.21}$$

where c_1,c_2 and c_3 are numerical parameters; discussions about the derivation of these formulation can be found in Ref.[50]. We could rewrite the split equation in the following way,

$$(v_h, \frac{\partial c_h}{\partial t} + \frac{\partial \tilde{c}}{\partial t}) + B(c_h, v_h) + (\tilde{c}, L^*(v_h))_h = < v_h, f > + (v_h, F)_{\Gamma_N} \quad \forall v_h \in \mathcal{V}_h \tag{4.22}$$

$$(\tilde{v}, \frac{\partial c_h}{\partial t} + \frac{\partial \tilde{c}}{\partial t}) + (\tilde{v}, \mathcal{L}(c_h))_h + \tau_{c_h}^{-1}(\tilde{v}, \tilde{c}) = < \tilde{v}, f > \quad \forall \tilde{v} \in \tilde{\mathcal{V}}_h \tag{4.23}$$

Note that in Eq.4.23 the values of $\tilde{c}$ on the element boundaries are neglected. Intuitively, it is necessary to solve for $\tilde{c}$ in oder to have the final solution c_h, but $\tilde{c}$ is unknown. However, rather than solving for $\tilde{c}$, we could give a closed-form expression according to Eq.4.23 and substitute it into Eq.4.22. Denote $\tilde{P}$ the L^2 projection onto the space of sub-scales; the equation used to solve for the sub-grid scale can be formally expressed as,

$$\tilde{P}[\frac{\partial \tilde{c}}{\partial t} + \tau_{c_h}^{-1}\tilde{c}] = \tilde{P}[f - \frac{\partial c_h}{\partial t} - \mathcal{L}(c_h)] \tag{4.24}$$

There are two main options for the choices of $\tilde{P}$ in order to construct the sub-scale spaces. The first and the most common option in the literature is to take the residual as the sub-scale spaces, and in this case, $\tilde{P} = I$ is the identity.

Another possibility is to make the sub-scales space orthogonal to the finite element space; the basic idea is to make the sub-scale method activated in regions where the solution cannot be resolved by the finite element space. In

this case, the projection operator is defined as $\tilde{P} = P^{\perp} = I - P_h$ with P_h being the projection on the finite element space. To simplify further the numerical method, we make additional approximations within each element:

$$P^{\perp}(f) \approx 0 \tag{4.25}$$

$$P^{\perp}(\nabla \cdot (D\nabla c_h)) \approx 0 \tag{4.26}$$

Eq.4.25 implies that f belongs to the finite element space $\mathcal{V}_h$ only or it is approximated by a finite element space. Refering to Eq.4.26 it simplifies the implementation of the method. We do not neglect the orthogonal parts of the convective term since this is the term that helps enhance the stability. Moreover, we have the following equalities because c_h is the solution on the finite element space and the sub-scale space is orthogonal to the finite element space:

$$P^{\perp}(\frac{\partial c_h}{\partial t}) = 0, \quad P^{\perp}(sc_h) = 0, \quad (v_h, \frac{\partial \tilde{c}}{\partial t}) = 0, \quad (\tilde{v}, \frac{\partial c_h}{\partial t}) = 0 \tag{4.27}$$

Finally we shall have the following simplified form for Eq.4.24,

$$\frac{\partial \tilde{c}}{\partial t} + \tau_{c_h}^{-1}\tilde{c} = P^{\perp}[-\boldsymbol{a} \cdot \nabla c_h] \tag{4.28}$$

Eq.4.28 provides a way to approximate the sub-scale solution $\tilde{c}$, which could be plugged in Eq.4.22. We could call the sub-scales dynamic if the temporal derivative, $\frac{\partial \tilde{c}}{\partial t}$, is taken into account. And in order to track the sub-scales in time a temporal discretization method, like the θ-method, could also be adopted here. Otherwise, there is another possibility of tracking the sub-scales in time by as asuming they are "quasi-static", meaning $\frac{\partial \tilde{c}}{\partial t} \approx 0$. Here, if we use the quasi-static form,

$$(v_h, \frac{\partial c_h}{\partial t}) + B(c_h, v_h) + \tau_{c_h}(P^{\perp}(-\boldsymbol{a}\cdot\nabla c_h), \boldsymbol{a}\cdot\nabla v_h)_h = < v_h, f > + (v_h, F)_{\Gamma_N} \quad \forall v_h \in \mathcal{V}_h \tag{4.29}$$

After temporal discretization, the stabilized form is,

$$(v_h, \frac{\triangle c_h}{\triangle t}) + \theta B(\triangle c_h, v_h) + \underbrace{\sum_{e=1}^{n_{element}} \tau_{c_h}(P^{\perp}(-\boldsymbol{a}^{n+\theta} \cdot \nabla c_h^{n+\theta}), \boldsymbol{a}^{n+\theta} \cdot \nabla v_h)}_{\text{Stabilization term}}$$

$$= -B(c_h^n, v_h) + < v_h, \theta f^{n+1} + (1-\theta) f^n > + (v_h, \theta F^{n+1} + (1-\theta)F^n)_{\Gamma_N} \quad \forall v_h \in \mathcal{V}_h \tag{4.30}$$

Stability and convergence properties have been discussed in Ref.[56]. We strongly favor the choice of the sub-scale spaces orthogonal to the finite element space, and advantages of this formulation are as follows,

- Relationship between the temporal step size and mesh size are not required, which make it possible to use anisotropic space-time discretization.
- Instabilities disappear for small temporal step size.
- τ_c is independent of the temporal step size.

With these advantages, we are going to use this variational multi-scale stabilization method, Eq.4.30, for our problem in order to yield a stable solution.In summary, the complete procedure for solving the TCDR equation is shown in algorithm 1, where we follow the θ method for temporal discretization and the Galerkin finite element method for spatial discretization. However, an internal iteration appears just in case there exist any nonlinear coefficients.

Algorithm 1 Algorithm for solving the TCDR equation

1: **for** $n = 0, ..., N-1$ **do**

2: $i \leftarrow 0$

3: Initialize the unknown :

$$c_h^{n+1,i} \leftarrow c_h^n$$

4: **while** not converged **do**

5:

- Compute the stabilization parameter:

$$\tau_{c_h}^{n+1} = (c_1 \frac{D}{h^2} + c_2 \frac{|\boldsymbol{a}^{n+1}|}{h} + c_3 s)^{-1}$$

$$\tau_{c_h}^{n} = (c_1 \frac{D}{h^2} + c_2 \frac{|\boldsymbol{a}^{n}|}{h} + c_3 s)^{-1}$$

- Compute $c_h^{n+1,i}$ by solving:

$$\begin{aligned}
&(v_h, \frac{c_h^{n+1,i}}{\triangle t}) + \theta B(c_h^{n+1,i}, v_h) + \theta \tau_{c_h}^{n+1}(P^{\perp}(-\boldsymbol{a}^{n+1} \cdot \nabla c_h^{n+1,i}), \boldsymbol{a}^{n+1} \cdot \nabla v_h) \\
&= (v_h, \frac{c_h^{n}}{\triangle t}) - (1-\theta) B(c_h^{n}, v_h) - (1-\theta)\tau_{c_h}^{n}(P^{\perp}(-\boldsymbol{a}^{n} \cdot \nabla c_h^{n}), \boldsymbol{a}^{n} \cdot \nabla v_h) \\
&+ < v_h, \theta f^{n+1} + (1-\theta) f^n > + (v_h, \theta F^{n+1} + (1-\theta) F^n)_{\Gamma_N} \quad \forall v_h \in \mathcal{V}_h
\end{aligned}$$

6: Set up converged values :

$$c_h^{n+1} \leftarrow c_h^{n+1,i}$$

4.4 Discretization of the Navier-Stokes equations

The Navier-Stokes equations are also approximated through the finite element method, but before this, we shall summarize the main difficulties involved in the numerical solution of incompressible flow problems.

The first difficulty is arising from the presence the non-symmetric and nonlinear convective term in Eq.3.35. Such problem could result in significant difficulty in flow of high Reynolds number, which are convection dominated. So the lack of numerical diffusion after the standard Galerkin formulation will again cause the solution to be unstable. Stabilization techniques as mentioned in the previous section must be used to provide a stable finite element solution at high Reynolds numbers.

Another complex part we have to tackle is the incompressibility condition, which actually is the continuity equation by assuming the constant flow density. This incompressibility condition implies the velocity field must be divergence free. On the other hand, the gradient of the pressure term works with the aim of introducing an additional degree of freedom required to satisfy the incompressibility condition. The pressure could adjust, immediately and interactively, itself corresponding to the change of velocity field so as to meet the divergence-free condition for the velocity. The pressure can be regarded as a Lagrange multiplier of the incompressibility condition and coupled with the velocity field.

4.4.1 Spatial discretization

Following a similar procedure as for the TCDR equation, the weak form of the Navier-Stokes equations could be obtained after integration by parts, and the variational problem becomes: find $[\boldsymbol{v}, p] \in \mathcal{S} \times \mathcal{Q}$, for all $[\boldsymbol{w}, q] \in \mathcal{V} \times \mathcal{Q}$ that

$$\begin{cases} (\boldsymbol{w}, \partial_t \boldsymbol{v}) + (\nu \nabla \boldsymbol{v}, \nabla \boldsymbol{w}) + (\boldsymbol{v} \cdot \nabla \boldsymbol{v}, \boldsymbol{w}) - (p, \nabla \cdot \boldsymbol{w}) = < \boldsymbol{w}, \boldsymbol{b} > + < \boldsymbol{w}, \boldsymbol{t} >_{\Gamma_N} \\ (q, \nabla \cdot \boldsymbol{v}) = 0 \end{cases} \tag{4.31}$$

Let us introduce the following notations:

$$V = [\boldsymbol{v}^T, p]^T \quad W = [\boldsymbol{w}^T, q]^T$$

,

$$L(V) = \begin{bmatrix} \boldsymbol{v} \cdot \nabla \boldsymbol{v} - \nabla(\nu \cdot \nabla \boldsymbol{v}) + \nabla p \\ \nabla \cdot \boldsymbol{v} \end{bmatrix}$$

$$B(V, W) = \begin{bmatrix} (\nu \nabla \boldsymbol{v}, \nabla \boldsymbol{w}) + (\boldsymbol{v} \cdot \nabla \boldsymbol{v}, \boldsymbol{w}) - (p, \nabla \cdot \boldsymbol{w}) \\ (q, \nabla \cdot \boldsymbol{v}) \end{bmatrix}$$

$$M := \begin{bmatrix} \boldsymbol{I}_{d\times d} & \mathbf{0}_{d\times 1} \\ \mathbf{0}_{1\times d} & 0 \end{bmatrix} \quad G := \begin{bmatrix} \boldsymbol{b} \\ 0 \end{bmatrix}$$

where $\boldsymbol{I}$ is the identity matrix with d the number of dimension. After integration by parts, rewrite Eq.4.31 in the following form

$$(W, M\partial_t V) + B(V, W) =< W, G > \tag{4.32}$$

We are also assuming $\boldsymbol{t} = \mathbf{0}$ for simplification of the notation, but we will introduce $\boldsymbol{t}$ in the final formulation.

The finite element approximation for this continuous problem requires first the partition of the computational domain as $\{\Omega^e\}_{e=1}^{n_{el}}$ whose characteristic length is denoted by h. So the weak form in Eq.4.31 can be approximated by the Galerkin method in finite dimensional spaces: find $V_h \in \mathcal{S}_h \times \mathcal{Q}_h$, such that for all $W_h \in \mathcal{V}_h \times \mathcal{Q}_h$

$$(W_h, M\partial_t V_h) + (W_h, L(V_h)) =< W_h, G > \tag{4.33}$$

Eq.4.33 is the Galerkin finite element discretization in space, which is very similar to the spatially discretized TCDR equation given in Eq.4.5. But apart from being unstable in the convection dominant case, Eq.4.33 has also to follow the inf-sup or Babuska-Brezzi condition[57], which requires to use the mixed interpolation, i.e., different interpolation spaces for $\boldsymbol{v}$ and p, and verifying

$$inf_{q_h\in\mathcal{Q}_h} sup_{\boldsymbol{v}_h\in\mathcal{S}_h} \frac{(q_h, \nabla\cdot\boldsymbol{v}_h)}{||q_h||||\boldsymbol{v}_h||} \geq \alpha > 0 \tag{4.34}$$

for a constant α independent of h.
Once the temporal discretization based on the finite difference method is introduced, the problem still suffers from different kinds of the instabilities part of which have been noted in previous. As we have already known the advantages of the variational multi-scale stabilization technique, we will introduce this method as the only stabilization method for the Navier-Stokes equations.

4.4.2 Temporal discretization

To track the transient response, the Navier-Stokes equations can be advanced in time by suitable finite difference schemes, such as the θ family methods introduced in the previous section. Note that a fully implicit method requires the solution of a nonlinear algebraic system at each time step. Semi-implicit methods in which the nonlinear convection term is treated explicitly are sometimes preferred.

4.5 Stabilization techniques for the Navier-Stokes equations

The initial idea for the variational multi-scale form here is similar to that we implemented in the TCDR equation. Firstly, let us decompose the continuous trial solution spaces $(\mathcal{S} \times \mathcal{Q})$ problem into two spaces which are orthogonal to each other, $(\mathcal{S} \times \mathcal{Q}) = (\mathcal{S}^h \times \mathcal{Q}^h) \oplus (\tilde{\mathcal{S}} \times \tilde{\mathcal{Q}})$, and $(\mathcal{S}^h \times \mathcal{Q}^h) \cap (\tilde{\mathcal{S}} \times \tilde{\mathcal{Q}}) = 0$, where the space $(\mathcal{S}^h \times \mathcal{Q}^h)$ is the finite element space and $(\tilde{\mathcal{S}} \times \tilde{\mathcal{Q}})$ is the sub-scale space.

To solve the Navier-Stokes equations using the variational multi-scale method, we could split the continuous problem in the following way,

$$V = V_h + \tilde{V} \tag{4.35}$$

where V belongs to the finite element space and $\tilde{V}$ belongs to the sub-scale space.

Correspondingly, the space $(\mathcal{V} \times \mathcal{Q}) = (\mathcal{V}^h \times \mathcal{Q}^h) \oplus (\tilde{\mathcal{V}} \times \tilde{\mathcal{Q}})$, and therefore $W = W_h + \tilde{W}$ with W belonging to the finite element space and $\tilde{W}$ belonging to the sub-scale space. The continuous problem now becomes,

On finite element space:

$$(W_h, M\partial_t V_h) + (W_h, M\partial_t \tilde{V}) + B(V_h, W_h) + (W_h, L(\tilde{V}))_h =< G, W_h > \tag{4.36}$$

On the orthogonal sub-scale space:

$$(\tilde{W}, M\partial_t V_h) + (\tilde{W}, M\partial_t \tilde{V}) + < \tilde{W}, L(V_h) > + < \tilde{W}, L(\tilde{V}) >=< G, \tilde{W} > \tag{4.37}$$

Considering the orthogonal property and also assuming G is directly on the finite element space or could be approximated by a function in the finite element space, the following equity holds,

$$(W_h, M\partial_t \tilde{V}) = 0 \quad (\tilde{W}, M\partial_t V_h) = 0 \quad < G, \tilde{W} >= 0 \tag{4.38}$$

The problems on finite element space and on sub-scale space have the following form, respectively,

$$(W_h, M\partial_t V_h) + B(V_h, W_h) + (W_h, L(\tilde{V}))_h =< G, W_h > \tag{4.39}$$

$$(\tilde{W}, M\partial_t \tilde{V}) + (\tilde{W}, L(V_h))_h + (\tilde{W}, L(\tilde{V}))_h =< G, \tilde{W} > \tag{4.40}$$

On the finite element space, we could obtain the weak form through integration by parts:

$$\begin{cases} (\boldsymbol{w}_h, \partial_t \boldsymbol{v}_h) + (\nu \nabla \boldsymbol{v}_h, \nabla \boldsymbol{w}_h) + (\boldsymbol{v} \cdot \nabla \boldsymbol{v}_h, \boldsymbol{w}_h) - (p_h, \nabla \cdot \boldsymbol{w}_h) \\ \qquad + \nu \sum_{e=1}^{n_{element}} [-(\tilde{\boldsymbol{v}}, \nabla^2 \boldsymbol{w}_h) + \underbrace{(\tilde{\boldsymbol{v}}, \boldsymbol{n} \cdot \nabla \boldsymbol{w}_h)_{\partial\Omega_e}}_{0}] \\ \qquad + \sum_{e=1}^{n_{element}} [-(\tilde{\boldsymbol{v}}, \boldsymbol{v} \cdot \nabla \boldsymbol{w}_h) + \underbrace{(\tilde{\boldsymbol{v}}, \boldsymbol{v} \cdot \boldsymbol{n} \boldsymbol{w}_h)_{\partial\Omega_e}}_{0}] \\ \qquad - \sum_K (\tilde{p}, \nabla \cdot \boldsymbol{w}_h) =< \boldsymbol{b}, \boldsymbol{w}_h > \\ (q_h, \nabla \cdot \boldsymbol{v}_h) - \sum_K (\nabla q_h, \tilde{\boldsymbol{v}}) + \underbrace{(q_h, \boldsymbol{n} \cdot \tilde{\boldsymbol{v}})_{\partial\Omega_e}}_{0} = 0 \end{cases} \tag{4.41}$$

where we have already substituted the fact $\nabla \cdot (\boldsymbol{v}_h + \tilde{\boldsymbol{v}}) = 0$ and have also assumed that the sub-scale solutions vanish at the all element boundaries, so terms involving integrals over these boundaries equal to 0 as it has been noted in Eq.4.41. Our purpose is to solve for $\boldsymbol{v}_h$ in Eq.4.41, but we have the unknowns $\tilde{\boldsymbol{v}}$ and $\tilde{p}$ which are necessary to be approximated on the sub-scale spaces from,

$$\begin{cases} (\tilde{\boldsymbol{w}}, \partial_t \tilde{\boldsymbol{v}}) - (\tilde{\boldsymbol{w}}, \nabla \cdot (\nu \nabla \tilde{\boldsymbol{v}})) + (\tilde{\boldsymbol{w}}, \boldsymbol{v} \cdot \nabla \tilde{\boldsymbol{v}}) + (\tilde{\boldsymbol{w}}, \nabla \tilde{p}) \\ \qquad + (\tilde{\boldsymbol{w}}, \partial_t \boldsymbol{v}_h) - (\tilde{\boldsymbol{w}}, \nabla \cdot (\nu \nabla \boldsymbol{v}_h)) + (\tilde{\boldsymbol{w}}, \boldsymbol{v} \cdot \nabla \boldsymbol{v}_h) \\ \qquad + (\tilde{\boldsymbol{w}}, \nabla p_h) =< \boldsymbol{b}, \tilde{\boldsymbol{w}} > \\ (\tilde{q}, \nabla \cdot \tilde{\boldsymbol{v}}) + (\tilde{q}, \nabla \cdot \boldsymbol{v}_h) = 0 \end{cases} \tag{4.42}$$

So the problem we are solving could be understood as,

$$\begin{cases} \partial_t \tilde{\boldsymbol{v}}_h + \nabla \cdot (\nu \nabla \tilde{\boldsymbol{v}}) + \boldsymbol{v} \cdot \nabla \tilde{\boldsymbol{v}} - \nabla \tilde{p} = \boldsymbol{r}_{v,h} \\ \nabla \cdot \tilde{\boldsymbol{v}} = r_{p,h} \end{cases} \tag{4.43}$$

where $\boldsymbol{r}_{v,h}$ and $r_{p,h}$ are the residuals of the finite element approximation $\boldsymbol{v}_h$ and p_h projected on the sub-scale space. Following the work in Ref.[58],Eq.4.43 could be approximated by introducing two stabilization parameters τ_1 and τ_2,

$$\begin{cases} \partial_t \tilde{\boldsymbol{v}} + \tau_1^{-1} \tilde{\boldsymbol{v}} = \boldsymbol{r}_{u,h} \\ \tilde{p} = \tau_2^{-1} r_{p,h} \end{cases} \tag{4.44}$$

where

$$\begin{cases} \boldsymbol{r}_{v,h} = P^{\perp}(\boldsymbol{b} - \partial_t \boldsymbol{v}_h + \nabla \cdot (\nu \nabla \boldsymbol{v}_h) - \boldsymbol{v} \cdot \nabla \boldsymbol{v}_h - \nabla p_h) \\ r_{p,h} = P^{\perp}(-\nabla \cdot \boldsymbol{v}_h) \\ \tau_1 = (c_1 \frac{\nu}{h^2} + c_2 \frac{|\boldsymbol{v}|}{h})^{-1} \\ \tau_2 = \frac{h^2}{c_1 \tau_1} \end{cases} \tag{4.45}$$

As we did in the variational multi-scale stabilized TCDR equation, in addition to neglecting the second order derivative accounting for the diffusion part, we observe that,

$$P^{\perp}(\boldsymbol{b}) = 0 \quad P^{\perp}(\partial_t \boldsymbol{v}_h) = 0 \tag{4.46}$$

The original problem in variational form becomes,

$$\begin{cases} (\boldsymbol{w}_h, \partial_t \boldsymbol{v}_h) + (\nu \nabla \boldsymbol{v}_h, \nabla \boldsymbol{w}_h) + (\boldsymbol{v} \cdot \nabla \boldsymbol{v}_h, \boldsymbol{w}_h) - (p_h, \nabla \cdot \boldsymbol{w}_h) \\ \quad - \sum_{e=1}^{n_{element}} (\tilde{\boldsymbol{v}}, \boldsymbol{v} \cdot \nabla \boldsymbol{w}_h)_h - \sum_{e=1}^{n_{element}} (\tilde{p}, \nabla \cdot \boldsymbol{w}_h)_h =< \boldsymbol{b}, \boldsymbol{w}_h > \\ (q_h, \nabla \cdot \boldsymbol{v}_h) - \sum_{e=1}^{n_{element}} (\tilde{\boldsymbol{v}}, \nabla q_h)_h = 0 \end{cases} \tag{4.47}$$

Thus, the final version of the approximated sub-scales is,

$$\begin{cases} \partial_t \tilde{\boldsymbol{v}} + \tau_1^{-1} \tilde{\boldsymbol{v}} = -P^{\perp}(\boldsymbol{v} \cdot \nabla \boldsymbol{v}_h + \nabla p_h) \\ \tilde{p} = -\tau_2 P^{\perp}(\nabla \cdot \boldsymbol{v}_h) \end{cases} \tag{4.48}$$

Considering the temporal derivative, if we neglect the $\partial_t \tilde{\boldsymbol{v}}$, the sub-scales are called quasi-static. If we have quasi-static sub-scales, the stabilized finite element approximation is

$$\begin{cases} (\boldsymbol{w}_h, \dfrac{\partial \boldsymbol{v}_h}{\partial t}) + (\nu \nabla \boldsymbol{v}_h, \nabla \boldsymbol{w}_h) + (\boldsymbol{v} \cdot \nabla \boldsymbol{v}_h, \boldsymbol{w}_h) - (p_h, \nabla \cdot \boldsymbol{w}_h) \\ + \sum_{e=1}^{n_{element}} [(\tau_1 \mathcal{P}^{\perp}(\boldsymbol{v} \cdot \nabla \boldsymbol{v}_h), \boldsymbol{v} \cdot \nabla \boldsymbol{w}_h) + (\tau_2 \mathcal{P}^{\perp}(\nabla \cdot \boldsymbol{v}_h), \nabla \cdot \boldsymbol{w}_h)]_h \\ \qquad\qquad\qquad\qquad\qquad\qquad\qquad\qquad =< \boldsymbol{b}, \boldsymbol{w}_h > \\ (q_h, \nabla \cdot \boldsymbol{v}_h) + \sum_{e=1}^{n_{element}} (\tau_1 \mathcal{P}^{\perp}(\nabla p_h), \nabla q_h)_h = 0 \end{cases} \tag{4.49}$$

The fully designed variational stabilized formulation is given in algorithm 2. Firstly, we discretize the time into N small steps, and the solver starts to iterate at each time step. Inside each time step, due to nonlinear terms appear in the Navier-Stokes equations, the Picard method is introduced to tackle the nonlinearity, i.e. initializing the unknown with the solution from previous step. Then, the solver compute the stabilization parameters and the necessary orthogonal projections on the sub-scales. The sub-scales can be tracked in two main ways, quasi-static or dynamic. Finally, the updated solution is acquired through the θ method and the Galerkin finite element method.

Algorithm 2 Algorithm for solving the Navier-Stokes equations

1: **for** $n = 0, ..., N-1$ **do**

2: $i \leftarrow 0$

3: Initialize the unknown :

$$\boldsymbol{v}_h^{n+1,i} \leftarrow \boldsymbol{v}_h^n \quad \tilde{\boldsymbol{v}}^{n+1,i} \leftarrow \tilde{\boldsymbol{v}}^n \quad p_h^{n+1,i} \leftarrow p_h^n \quad \tilde{p}^{n+1,i} \leftarrow \tilde{p}^n$$

4: **while** not converged **do**

5:

- $i \leftarrow i+1$

$$\boldsymbol{v}_h^{n+\theta,i} \leftarrow \theta \boldsymbol{v}_h^{n+1,i} + (1-\theta)\boldsymbol{v}_h^n \quad \tilde{\boldsymbol{v}}^{n+\theta,i} \leftarrow \theta \tilde{\boldsymbol{v}}^{n+1,i} + (1-\theta)\tilde{\boldsymbol{v}}^n$$

$$p_h^{n+\theta,i} \leftarrow \theta p_h^{n+1,i} + (1-\theta)p_h^n \quad \tilde{p}^{n+\theta,i} \leftarrow \theta \tilde{p}^{n+1,i} + (1-\theta)\tilde{p}^n$$

- $\boldsymbol{v} \leftarrow \boldsymbol{v}_h^{n+\theta,i-1} + \tilde{\boldsymbol{v}}^{n+\theta,i-1}$
- Compute the stabilization parameters:

$$\tau_1 = (c_1 \frac{\nu}{h^2} + c_2 \frac{|\boldsymbol{v}|}{h})^{-1} \quad \tau_2 = \frac{h^2}{c_1 \tau_1} \quad \tau_{1t} = (\frac{1}{\theta \delta t} + \frac{1}{\tau_1})$$

- Compute the projections:

$$\xi_h = -\tilde{\mathcal{P}}(\boldsymbol{v} \cdot \nabla \boldsymbol{v}_h^{n+\theta,i-1}) \quad \zeta_h = -\tilde{\mathcal{P}}(\nabla p_h^{n+\theta,i-1}) \quad \delta_h = -\tilde{\mathcal{P}}(\nabla \cdot \boldsymbol{v}_h^{n+\theta,i-1})$$

- Update the sub-scales $\tilde{\boldsymbol{v}}^{n+\theta,i}$, $\tilde{p}^{n+\theta,i}$ with new $\boldsymbol{v}_h^{n+1,i}$ and $p_h^{n+1,i}$ by solving:
- **if** we use dynamic sub-scales **then**

$$\begin{cases} \frac{\tilde{\boldsymbol{v}}^{n+1,i} - \tilde{\boldsymbol{v}}^n}{\delta t} + \tau_1^{-1} \tilde{\boldsymbol{v}}^{n+\theta,i} = \xi_h + \zeta_h \\ \tilde{p}^{n+\theta,i} = \tau_2 \delta_h \end{cases}$$

- **else**

$$\tilde{\boldsymbol{v}}^{n+\theta,i} = \tau_1(\xi_h + \zeta_h) \quad \tilde{p}^{n+\theta,i-1} = \tau_2 \delta_h$$

- Compute $\boldsymbol{v}_h^{n+1,i}$ and $p_h^{n+1,i}$ by solving:

$$(\boldsymbol{w}_h, \frac{\boldsymbol{v}_h^{n+1,i} - \boldsymbol{v}_h^n}{\delta t}) + (\nu \nabla \boldsymbol{v}_h^{n+\theta,i}, \nabla \boldsymbol{w}_h) + (\boldsymbol{v} \cdot \nabla \boldsymbol{v}_h^{n+\theta,i}, \boldsymbol{w}_h) - (p_h^{n+\theta,i}, \nabla \cdot \boldsymbol{w}_h)$$
$$(q_h, \nabla \cdot \boldsymbol{v}_h^{n+\theta,i}) - \sum_K [(\tilde{\boldsymbol{v}}^{n+\theta,i}, \boldsymbol{v} \cdot \nabla \boldsymbol{w}_h + \nabla q_h) + (\tilde{p}^{n+\theta,i}, \nabla \cdot \boldsymbol{w}_h)]$$
$$= < \boldsymbol{b}, \boldsymbol{w}_h >$$

6: Set up converged values :

$$\boldsymbol{v}_h^{n+1} \leftarrow \boldsymbol{v}_h^{n+1,i} \quad \tilde{\boldsymbol{v}}^{n+1} \leftarrow \tilde{\boldsymbol{v}}^{n+1,i} \quad p_h^{n+1} \leftarrow p_h^{n+1,i} \quad \tilde{p}^{n+1} \leftarrow \tilde{p}^{n+1,i}$$

4.6 Shock capturing techniques

The previous stabilization techniques yield a globally stable solution in a convection dominant case, but local oscillations may still remain in domains where the solution exhibits sharp gradients. Although these oscillations might be neglected in linear problems, they may result in a global failure of iterative schemes, especially in nonlinear cases. Methods aiming to avoid these failure are usually termed "shock capturing" or "discontinuity capturing" techniques. The main idea for the shock capturing method is to add some artificial numerical diffusion (k) into the Galerking term of the finite element equation in the proximity of sharp gradients.

There are mainly two kind of non-linear methods in order to calculate the added diffusion terms. The first one the the so-called *Residual* based technique, which is consistent in the sense that if it is applied to the exact solution of the concentration c and the velocity $\boldsymbol{a}$, the residual is zero. The diffusion term is

$$k_{TCDR} = \frac{1}{2}\alpha h \frac{|R(c_h)|}{|\nabla c_h|} \tag{4.50}$$

$$k_{NS} = \frac{1}{2}\alpha h \frac{|R(\boldsymbol{v}_h)|}{|\nabla \boldsymbol{v}_h|} \tag{4.51}$$

Where k_{TCDR} and k_{NS} are the added diffusion with respect to the TCDR equation and the Navier-Stokes equation; α is a constant coefficient and the recommended value is usually 0.8 in the Ref.[59], and $R(\cdot)$ is the residual operator.

Another non-linear method is the weakly consistent *Orthogonal* projection technique[56], a different method consisting in adding an artificial diffusion which is proportional to the projection of the gradient onto the space orthogonal to the finite element space. The diffusion is active only in regions of sharp gradients which cannot be resolved by the finite element mesh, that is to say,

$$k_{TCDR} = \frac{1}{2}\alpha(|\boldsymbol{a}|h + sh^2)\frac{|P^{\perp}(\nabla c_h)|}{|\nabla c_h|} \tag{4.52}$$

$$k_{NS} = \frac{1}{2}\alpha(|\boldsymbol{v}|h)\frac{|P^{\perp}(\nabla \boldsymbol{v}_h)|}{|\nabla \boldsymbol{v}_h|} \tag{4.53}$$

In practice, the way to add these diffusion terms also varies if we consider the crosswind direction. The first option is to add the diffusion terms in an isotropic way, which is just to add the same artificial diffusion into all the diffusion components,recalling Eq.3.34, Eq.3.35, i.e,

$$D_{TCDR} = D + k_{TCDR} \quad \nu_{NS} = \nu + k_{NS} \tag{4.54}$$

The second method is to add the artificial diffusion in an anisotropic fashion. The initial idea is that the diffusion terms introduced by the stabilization method satisfies the requirements for eliminating the local oscillations, but they only added diffusion along the streamlines with quantities D_{ST} and ν_{ST}, excluding the numerical diffusion terms which have already been incorporated by the variational multi-scale stabilization method. The excluded terms could be roughly estimated as,

$$D_{SG} = \tau_c |\boldsymbol{a}|^2 \quad \nu_{SG} = \tau_{NS} |\boldsymbol{v}|^2 \tag{4.55}$$

So considering to maintain the stabilization, the added artificial diffusions are expressed as

$$D_{ST} = \max(0, k_{TCDR} - D_{SG}) \quad \nu_{ST} = \max(0, k_{NS} - \nu_{SG}) \tag{4.56}$$

Moreover, as previous research in Ref.[60] on the shock capturing method, the artificial diffusion should be introduced only in the crosswind direction. So the final version of the artificial diffusion terms considering both the variational multi-scale method and the shock capturing method is,

$$\boldsymbol{D}_{TCDR} = (\boldsymbol{I}D + \boldsymbol{O}k_{TCDR} + \boldsymbol{S}D_{ST}) \quad \boldsymbol{\nu}_{NS} = (\boldsymbol{I}\nu + \boldsymbol{O}k_{NS} + \boldsymbol{S}\nu_{ST}) \tag{4.57}$$

where $\boldsymbol{I}$ is the second order identity tensor; $\boldsymbol{S}$ is the streamline direction defined as

$$\boldsymbol{S} = \frac{\boldsymbol{v} \otimes \boldsymbol{v}}{|\boldsymbol{v}|^2}$$

and $\boldsymbol{O}$ is the orthogonal projector defined as $\boldsymbol{O} = \boldsymbol{I} - \boldsymbol{S}$.

In brief summary, we modify the original diffusion coefficients, D and ν, of the TCDR equation and the Navier-Stokes equations respectively, giving the the final diffusion terms considering both the streamline diffusion, D_{ST} and ν_{ST}, and crosswind diffusion k_{TCDR} and k_{NS}. However, after this modification, the original TCDR equation becomes a nonlinear equation, which explains why we put the internal iteration in algorithm 1.

Chapter 5

Validation of particle transport model

In this chapter, considering we have formulated so many equations in chapter 3, we validate the whole procedure and check whether it works as expected comparing our results with those in relevant literature. Firstly, the dust settling velocity is shown for a range of dust particles whose diameters will cause damages to health and environments. Besides, we implement our model in FEMUSS which is multiphysics simulation software written in Fortran 2003. Test cases are designed in order to verify the effectiveness of the code and the model. Numerical tests show that our model works very well and gives more accurate solutions than that did in the references. Further, the last dynamic case implies that our model works very well if the approximation parameters and boundary conditions are specified well.

5.1 Particle deposition

In chapter 3 we have given the particle settling velocity changes with respect to the dust properties we are especially interested the diameter. We plot the settling velocity of dust with diameters ranging from $0.1\mu\mathrm{m}$ to $100\mu\mathrm{m}$ because these particles have significant effect on human health and environment. The settling velocity logarithmicly changes according to the particle size as shown in figure 5.1.

TABLE 5.1: Parameters for computing settling velocity in different diameters

Particle density $\rho_p/\mathrm{kg}\cdot\mathrm{m}^{-3}$	Fluid density $\rho_a/\mathrm{kg}\cdot\mathrm{m}^{-3}$	Dynamic viscosity of fluids$\mu/\mathrm{Pa}\cdot\mathrm{s}$
2.5×10^{3}	1.18	1.8×10^{-5}

Other parameters such as the particle density and fluid density and dynamic viscosity in Eq.3.37 are shown in table 5.1, and we will use them also in other simulations without explicit statements. This settling velocity obtained can

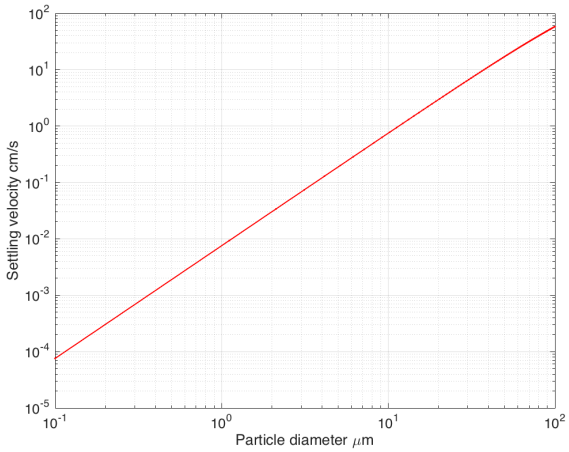

FIGURE 5.1: Particle settling velocity with different particle size

be verified from the experimental results shown in figure 4 of Ref.[61] in which the authors show comparisons between experimentally determined dry deposition velocities and deposition velocities calculated from theoretical approximations.

5.2 Numerical tests

The numerical tests are conducted in a square domain: $\Omega = [0, 5] \times [0, 5]$ as implemented in Ref.[20], which has been explained in chapter 3. Numerical results are compared in three cases: analytical solution, constant boundary condition and step-function boundary condition. We will see their behavior in this section. In all this test, the wind velocity profiles are assumed to be

$$U = \begin{cases} \frac{u_*}{k} \ln(z/z_0) & \text{for } z_0 < z < \delta \\ U_{\max} & \text{for } z \geq \delta \end{cases} \tag{5.1}$$

where U is the horizontal velocity; k is the von Karman constant. U reaches a maximum $U_{\max}$ at the boundary layer height $z = \delta(\approx 0.25\mathrm{m})$. The velocity profile inputted into the numerical code takes the boundary layer height effect into account as well. The diffusion coefficient is taken as constant above the boundary layer, $D = u_* k \delta$.

5.2.1 Femuss

Femuss is abbreviated for *Finite Element Method Using Subgrid Scales*, a program developed in our group for solving multi-physics problem using finite element methods. This powerful program written in *Fortran 2003*, is object oriented and now currently has been fully parallelized through MPI.

The idea for such program is to solve the multi-physics problem through the following procedures: a) the master node reads the data and after domain partition scatters the geometry, boundary conditions,etc. to all nodes; b) The numerical simulation starts in parallel. Global data required for the initial scattering is released from memory; c) The previous two steps need to be separated from each other in the program, so that the first one (involving many serial operations) is done in a local server and the second could be sent to the parallel cluster if necessary; d) at this point, the linear algebra solver library not only is used as a solver but also is in charge of the partitioning and communications between subdomains; e) after the problem is solved, the results are processed in GiD, a pre and post processor developed at CIMNE: http://www.cimne.com.

We implement our particle transport model in Femuss and show the numerical tests compared to the results in the literature as the validation.

5.2.2 Comparisons with analytical solutions

We can also compare our mathematical model with numerical solution to other analytical and numerical solution such as Roney and White's analytical model expressed in terms of Gamma Function as we discussed in chapter 3. In Ref.[20], Roney and White solve the problem with the parameters shown in table 5.2.

TABLE 5.2: Parameters for Roney and White's model

z_0/m	$u_*/\mathrm{m}\cdot\mathrm{s}^{-1}$	$C_0/\mathrm{mg}\cdot\mathrm{m}^{-3}$	$\mathrm{w/m}\cdot\mathrm{t}^{-1}$	β	m
0.0001	0.8	50	0.0024	14.277	0.2244

Both the numerical and analytical solutions appear to be very slowly approaching Gillette's hypothetical solution, which is valid only for $x \to \infty$. At $x = 5.0\mathrm{m}$ in the wind tunnel experiments, as expected, Gillette's analytical solution is not valid. The numerical solution here and Eltayeb and Hassan's analytical solution provide a better model for what one should expect when measuring the wind-tunnel concentration profiles. The numerical solutions are then compared to the data from the literature for the constant surface boundary condition in the next sections.

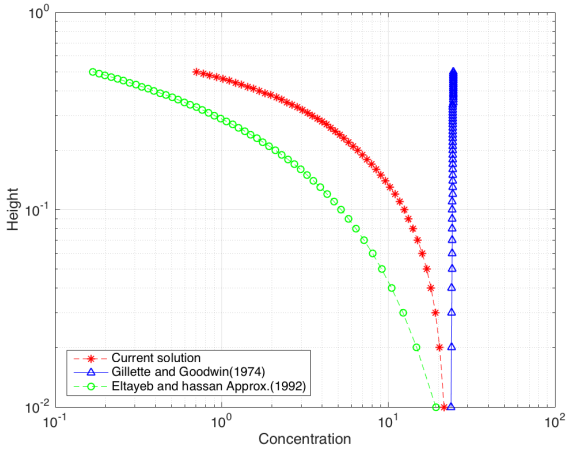

FIGURE 5.2: Solution comparisons for three different methods obtained from a constant concentration on surface at $x = 5\mathrm{m}$

5.2.3 Test of boundary with constant boundary conditions

We can still run more cases which have been implemented in Roney and White's work[20]. The boundary condition for this problem is defined with a slight modification of Eq.3.7,

$$\begin{cases} c(0,z) = 0.0 \\ c(x,\infty) = 0.0 \\ c(x,z_0) = F(x) \end{cases} \tag{5.2}$$

where we set the function $F(x)$ on the land surface boundary as a constant C_0 value. This cases happens when the near-surface flow reaches a steady state and the concentration remains constant for the same soil type. z_0 here appears because the concentration in Roney and white's work are obtained at that height, but that can be used to approximate the boundary concentration through experiments. So here we still keep this notation but shall keep in mind that $c(x, z_0)$ is the surface boundary concentration.

TABLE 5.3: Parameters for simulation with constant surface concentration

z_0/m	$u_*/\mathrm{m}\cdot\mathrm{s}^{-1}$	$C_0/\mathrm{mg}\cdot\mathrm{m}^{-3}$	$w/\mathrm{m}\cdot\mathrm{t}^{-1}$	β	m
0.00063	0.8	92	0.0024	14.277	0.2244

In figure 5.3, all the boundary conditions are clearly given according to the previous analysis. The surface concentration is fixed to $92\mathrm{mg/m}^3$. The numerical solution contour is shown in figure 5.4. The solution has largest value on the boundary and decrease smoothly to $0\mathrm{mg/m}^3$ as the height increases. This solution is the same as in figure 6 of Ref.[20].

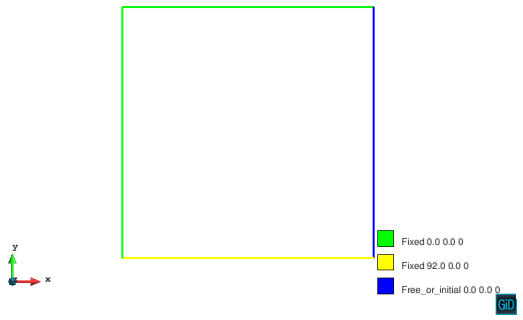

FIGURE 5.3: Boundary conditions for tests with constant surface concentration

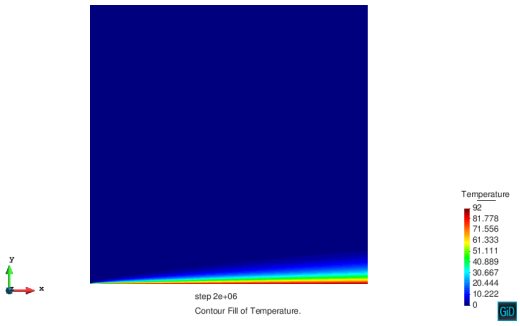

FIGURE 5.4: Dust concentration for tests with constant surface concentration

5.2.4 Test of boundary with step-function boundary conditions

A step-function boundary conditions was used to reproduce the North and South Sheet experimental simulations carried by Roney and White[62], which are designed for non-homogenous land surface (in terms of soil type) with sand soil placed upwind of a "loamy-type" soil. Two constant surface boundary were designed for this cases, $F(x) = C_{01}$ for the sand soil and $F(x) = C_{01}$ for the loamy soils. More formally, this simulations are designed with parameters given in table 5.4 when $F(x)$ is a step function,

$$F(x) = \begin{cases} C_{01} & \text{for } 0 \leq x \leq 2.65 \\ C_{02} & \text{for } 2.65 < x \leq 5.0 \end{cases} \tag{5.3}$$

TABLE 5.4: Parameters for simulation with step-function

z_0/m	$u_*/\mathrm{m}\cdot\mathrm{s}^{-1}$	$C_{01}/\mathrm{mg}\cdot\mathrm{m}^{-3}$	$C_{02}/\mathrm{mg}\cdot\mathrm{m}^{-3}$	$\mathrm{w/m}\cdot\mathrm{t}^{-1}$	β	m
0.00063	0.8	20	300	0.0024	14.277	0.2244

We choose the same parameters for the simulation as implemented by Roney and White[20] in order to validate our model. The boundary conditions are the same as in the previous test, except a small change on the land surface as in figure 5.5. On the left part on the surface, the concentration is fixed to $20\mathrm{mg/m}^3$ and the remaining part is fixed to $300\mathrm{mg/m}^3$ which are the so-called step-function boundary conditions. If we have more than two kind of soils on the surface, the step-function needs to be split into more sections, considering the number of soil types. Figure 5.6 is the concentration contours of the

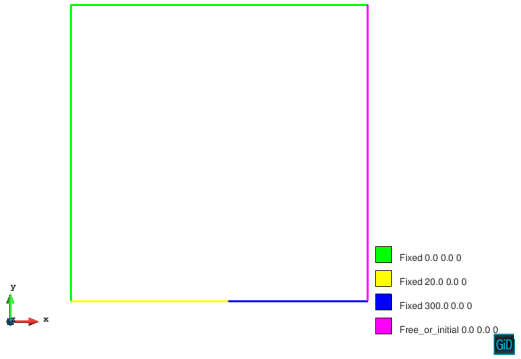

FIGURE 5.5: Boundary conditions for tests with step function on surface

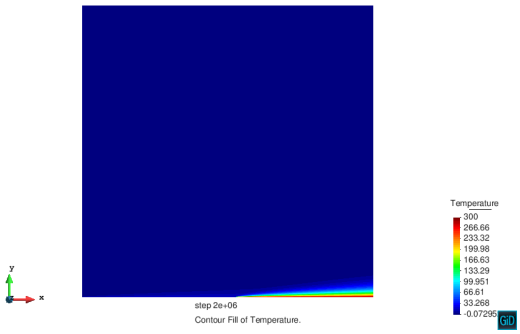

FIGURE 5.6: Dust concentration for tests with step function

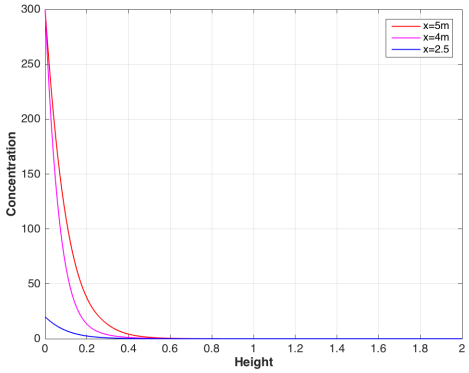

FIGURE 5.7: Dust concentration at selected downwind position

numerical solution for the case in which the surface boundary condition $F(x)$ is a step function. In order to show the different effect of the step function, we choose three downwind position and plot the result in figure 5.7. We can observe that although the surface concentrations could be different on the bottom due to soil types, they show a similar decreasing profile as the height goes up. The step-function solution is a boundary condition that does not readily lead itself to analytical solution; and thus, this case exemplifies the advantages of numerical solution. This solution here can also be compared to figure 10 of Ref.[20].

5.2.5 Test of dynamical model

With the previous validation, we here could try to show whether our model could capture the solution in a dynamic case which integrates all parts as we explained in chapter 3, solving particle transport problem coupled with Navier-Stokes problem. The simple model is sketched a square domain:

$\Omega = [0, 4] \times [0, 4]$. The bottom edge, the land surface, is the only boundary for generating particles during the erosion process, which means the vertical dust flux comes to work as an Neumann boundary condition. In the other boundary, there are no fluxes could cross the boundary. Considering the Navier-Stokes problem, we assign the inlet boundary on the bottom-left edge and outlet on the top-left edge, while in the remaining edges, the boundaries are assigned with slip wall boundary condition, figure 5.8. Initially, we give an inlet velocity increasing from $0\mathrm{m/s}$ to $\boldsymbol{v} = [5\mathrm{m/s}, 0]^{\mathrm{T}}$, and the outlet is free. At a given time, we stop the inlet flow in order to check if the settling process would happen,as in figure 5.9. Considering the concentration equation, we have known that we inject the clean flow on the inlet boundary, so the solution should be 0 on that place, figure 5.10. On the other hand, the bottom edge is the land surface, dust particles are generated due to the effect of flow erosion, and therefore, the boundary conditions there belongs to Neumann type.

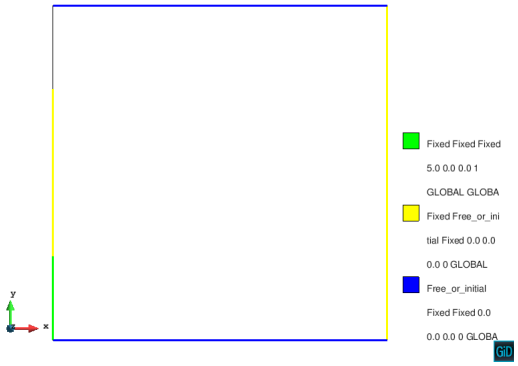

FIGURE 5.8: Boundary conditions for the Navier-Stokes equations in dynamic case

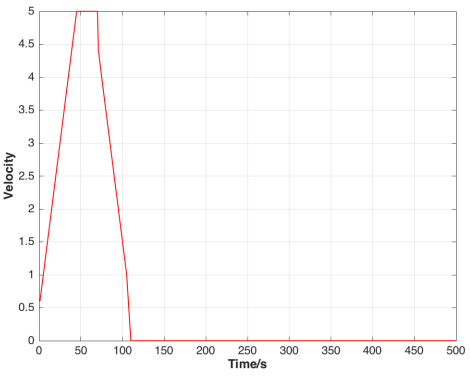

FIGURE 5.9: Velocity profile on the inlet boundary

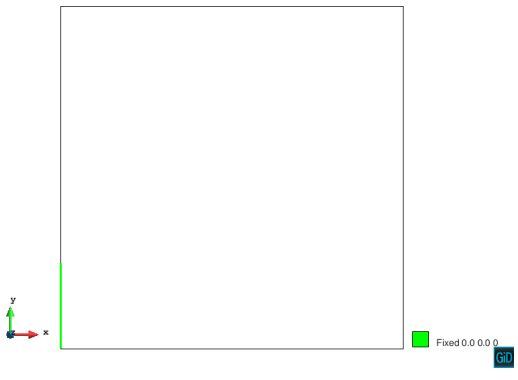

FIGURE 5.10: Dirichlet boundary conditions for concentration equation

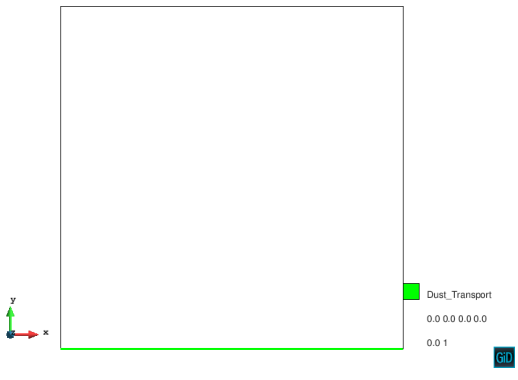

FIGURE 5.11: Neumann boundary conditions on land surface

We calculated the evolution of concentration from $0\mathrm{s}$ to $500\mathrm{s}$. Since we are unable to show the animations here, selected points, A, B, C and D, in the

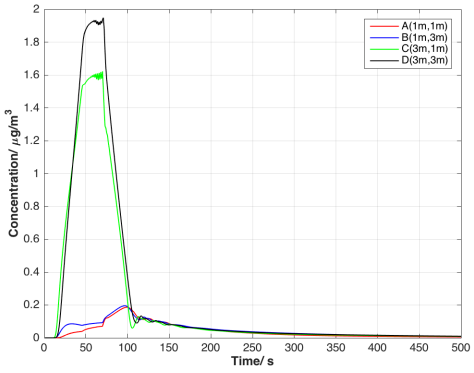

FIGURE 5.12: Dust concentration evolution for 4 selected points

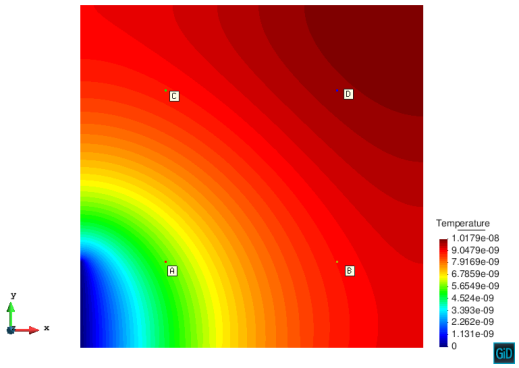

FIGURE 5.13: Dust concentration ($c/\mathrm{kg}\cdot\mathrm{m}^{-3}$) at $500s$

domain are extracted in order to show the solution evolution with respect to time, figure 5.12. We observe that in an initial stage, the concentration remains $0\mu\mathrm{g}\cdot\mathrm{m}^{-3}$, which is because the value of friction velocity on the land surface has not reached that of threshold friction velocity and therefore no vertical dust fluxes could be generated. And also because the dust requires time to propagate after the fluxes have entered the domain from the bottom edge. Increasing with the inlet flow velocity until $t = 45s$, the inlet velocity reaches its peak and remains steady until $t = 75\mathrm{s}$. During this time, the concentration also reaches its maximum. Later, when the velocity of the inlet flow starts to decrease, the concentration also decreases roughly to $0\mu\mathrm{g}\cdot\mathrm{m}^{-3}$ at $t = 500\mathrm{s}$, which means that the dust deposition formulation works very well. On the other hand, we can see that there two points,i.e. A and B, have very small concentration throughout the whole period. This is because the inlet is clean flow without any pollutants, and when the clean flow is injected into the domain, it is mixed with the dirty dust and carries it to the outlet edge. Figure 5.13 gives a very clear contour of the concentrations in the whole computational domain at $t = 500\mathrm{s}$.

At the end of these tests successfully implemented, we have validated our solution with respect to analytical solutions and also, depending the requirements of the simulated problems, the numerical solutions with different boundary conditions from the model of Roney and White[20]. Our code works very well. The last dynamic case shows the mechanism of the dust generation and dust deposition process in small flow velocity.

Chapter 6

Numerical simulation of wind tunnel

In this chapter, we give a brief introduction to wind tunnel. Besides, we also explain how dust particles are settled in the atmosphere and this should be observed by wind tunnel experiment. However, wind tunnel experiment has a strict requirement for the instrument, so we apply our theoretical model, instead of real experiments, to approximate the dust dynamics in a large domain.

6.1 Problem introduction

6.1.1 Wind tunnel experiment

The wind tunnel is widely used in aerodynamics to produce the desired flow field with specifically controlled conditions if necessary. Based on the flow speed, there are four kind of wind tunnels: supersonic or low speed wind tunnels, $M \ll 1.0$; transonic wind tunnels, $M \approx 1.0$; supersonic wind tunnels, $1.0 < M < 5.0$; hypersonic wind tunnels, $M > 5.0$.

On the other hand, atmospheric pollution is generated primarily from the spewing of gasses and erosive land which can release particles into the atmosphere. If these particles are heavy enough and also the windspeed is not too large, they will fail to reach a suspended status in atmosphere. However, if the particles were very fine and carried by violent wind, they would rise a certain distance, travel with the wind and then descend slowly. For example, airborne dust particles can be transported thousands of kilometers from their source region, therefore the interaction of dust aerosols with their components of the Earth system produces a wide range of often complex impacts on ecosystems, weather and climate, hydrological cycle, agriculture, and human health.

Existing methods used to simulate particle transport are based mainly on wind tunnel experiments. A recent review of Robert[63] summarized research on the dust source and focus mainly on dust emission processes in

terms of quantification, landforms and geomorphology. Many experiments use the passive sampling method, i.e. with instruments not provided with flow meters to collect the dust particles, during which many particles are emitted from the soil [64]. The advantage of passive samplers is that they operate mechanically and are much cheaper than active samplers so that many locations can be sampled at a reasonable cost[65]. They allow one to collect considerable quantities of sediment, sometimes grams and more, which can later be analyzed for grain size distribution, chemical composition, biological content, and other analyses. The measurements of dust flux by wind remain one of the most problematic procedure in our Earth system but also necessary to assess the intensity of dust particles in a given environment, especially the horizontal and vertical flux. In order to obtain correct flux data, we require that the instruments have sufficient efficiency and enough accuracy, but this is not practical especially in no-windy conditions[66].

6.1.2 Numerical experiment

Instead of an real wind tunnel experiment, we here could apply our dust transport model with approximate boundary conditions to the simulation of dynamics of dust with diameters $10\mu\mathrm{m}$ in a certain domain, which shall also be able to reproduce the results as from the real tunnel experiment. The flux formulation,Eq. 3.28, used is Shao's 2004 scheme and specific parameters are given in Appendix A

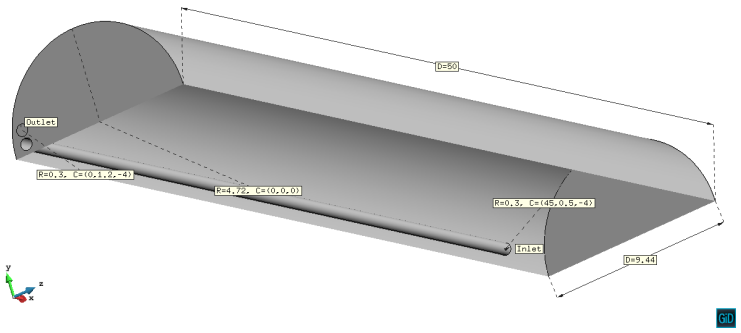

FIGURE 6.1: Dimensional drawing of the wind tunnel model

Figure 6.1 is the wind tunnel model in which we are going to conduct our dust transport model. We can see that the length and height of such wind tunnel are $50m$ and $4.72m$, respectively. In order to show the internal structure of the wind tunnel, the bottom surface has been removed temporally, but we should keep in mind that our domain is a closed domain in 3D. The conditions for flow and dust transport are assigned independently as,

1. Boundary conditions for Navier-Stokes equations. There exists a tube to define the inlet flow which has been marked by the keyword "Inlet" in the figure, and correspondingly, another small circle on the surface is labeled by the keyword "Outlet". Other boundaries for the flow are assigned with slip boundary conditions, so the flow can only be injected

through the inlet boundary by a given velocity, and leave the domain through ony the outlet boundary.

2. Boundary conditions for TCDR equation. In the wind tunnel, we have to assign the the bottom edge as the land surface, so when the flow moves over the surface with a friction velocity lager than the threshold friction velocity, the dust will be generated then enters the domain with the vertical dust flux.

3. Initial conditions. Initially the flow velocity is $[0\mathrm{m}\cdot\mathrm{s}^{-1}, 0, 0]^{\mathrm{T}}$ in the whole domain and therefore the dust is zero according to the erosion condition. However, the inlet velocity keeps increase to $[30\mathrm{m}\cdot\mathrm{s}^{-1}, 0, 0]^{\mathrm{T}}$ and the friction velocity will reach the threshold friction velocity, and the dust is generated. The coupled system remains in this status until the friction velocity is smaller that threshold. We stop the injected flow after a while in order to see the dust settling down on the land surface.

6.2 Simulation results

We simulate the whole wind tunnel with a time scale from $0\mathrm{s}$ to $600\mathrm{s}$. The dust concentration shows a similar dynamical behavior as we see in the last test of chapter 5. At an initial stage, the dust is 0 because the friction velocity has not reached the threshold friction velocity. As the friction velocity increases, vertical fluxes on the land surface are activated on the corresponding land surface. In figure 6.2, we can observe the dust concentration profiles in the wind tunnel. It is interesting that the largest dust concentration is located near the inlet boundary, which is because the flow has a relatively large velocity compared to that of other place as shown in figure 6.3. Because the inlet flow drop linearly to $[0\mathrm{m}\cdot\mathrm{s}^{-1}, 0, 0]^{\mathrm{T}}$ at $t = 60\mathrm{s}$, so the flow would remain motional due to the inertia.

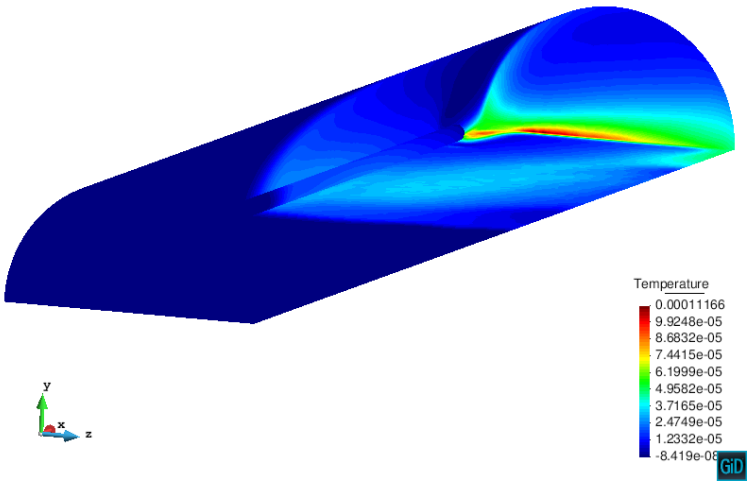

FIGURE 6.2: Dust concentration in wind tunnel at $t = 14\mathrm{s}$

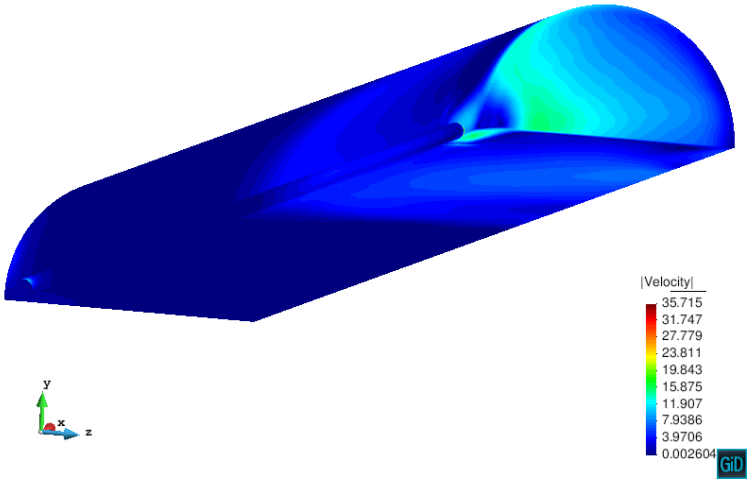

FIGURE 6.3: Flow velocity in wind tunnel at $t = 14$s

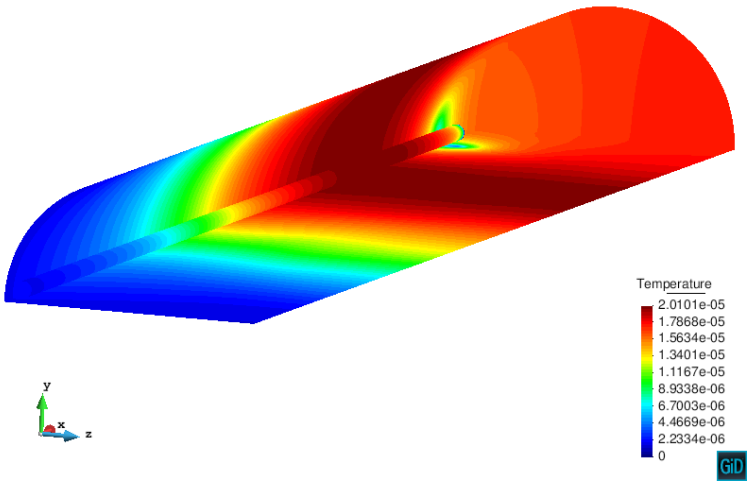

FIGURE 6.4: Dust concentration in wind tunnel at $t = 600$s

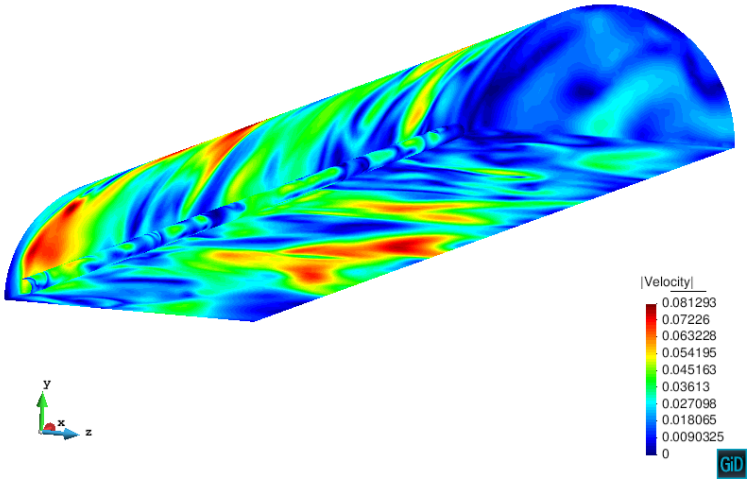

FIGURE 6.5: Flow velocity in wind tunnel at $t = 600\text{s}$

In figure 6.5 we see that the flow velocity has decreased to a steady state. And we can image that if the model had been simulated with a longer time scale, it might be possible for us to find the flow in static status. The only convection velocity for the dust concentration is the settling velocity. Figure 6.4 is the corresponding dust concentration distributed in the domain, where the internal places have a relatively larger dust concentration which is convected by wind flow to the outlet boundary. However, because the inlet flow is stopped, as we have explained, the dust fails to reach the outlet boundary, and all the quantity dust eroded from the bottom surface has to be conservative in the wind tunnel and waits to settle down with the settling velocity. For the particle in our simulation, diameter as $10\mu\text{m}$, the theoretical settling velocity is $6.3 \cdot 10^{-3}\text{m/s}$, which is negligible compared to flow velocity as shown in figure 6.5, meaning that it requires a very long term for the particles to settle down. During this time, the dust remains floating in the air. This is also the reason why we find many cities suffer from fog storm or suspended particles.

Chapter 7

Conclusions

In the following chapter, the main contributions of this thesis are summarized and research lines for future development are presented.

7.1 Contributions

The objective of this work, to develop a numerical model for the transport of dust particles in fluids considering the gravitational effects, has been achieved with the assistance of the finite element and finite difference methods.

The main contributions of the thesis can be summarized as follows.

1. Explanations of dust erosion mechanism. Erosion processes are affected many factors including the soil properties and flow velocity. The land surface erosion is initiated when when the friction velocity is larger than the threshold friction velocity. The value of threshold friction velocity depends on the property of dust particles, e.g., diameters, soil moisture and surface land roughness,etc. Once the land surface is eroded by injected flow, the dust entering into the domain can be quantized through an approximation of horizontal flux and vertical flux which are formulated explicitly through experimental data fitting. Once the flux in available, the concentration dynamics in the domain can be described through the unsteady convection-diffusion equation.
2. Stabilized finite element formulations for TCDR equation and incompressible Navier-Stokes equations. The complexity of the mathematical problem makes their numerical solution very difficult. Despite the important incompressibility condition which is tackled a Lagrange multiplier, the nonlinear convection term appearing in Navier-Stokes equation make the numerical approximation much more difficult. A variational multiscale finite element approximation for coupled TCDR and Navier-Stokes equations is described in partitioned manner. The subscales were considered as transient and orthogonal, keeping the effect of the sub-scales both in the nonlinear convective terms of the momentum equations. Considering in real engineering case, the concentration may have large gradient if some regions, the shock capturing methods,

adding more numerical diffusion in the crosswind direction, are also extended to the problem which leads to more accurate solutions.

3. Numerical simulation of dust transport in wind tunnel. This simulation helps restore what actually happens in a our environmental atmosphere. Dust particles are generated in regions where the wind has relatively large velocity and then the dust can be convected to the downwind direction, thereby polluting more regions. They also take a long term to settle down onto the ground because the deposition velocity is almost negligible compared to that of the wind. So people are easily to be exposed to these harmful extent and suffer from health issues. And it can cause other corresponding adverse effects on the environment.

7.2 Future developments

7.2.1 Extension to dust with mixed diameters

Depending on the soil type, there is usually a larger amount of dust which is not "free" but contained in aggregates and can be released only through mechanical destructions. It is therefore necessary to estimate the fraction of dust particles in terms of different size. In the model, all the dust particles are assumed to have the same diameters after eroded by medium flow. This hypothesis does not really holds in an real situation where the particle diameters are distributed among a certain range[2, 4].

7.2.2 Adaptive mesh refinement

Complex flow features, like shock and boundary layers require different mesh sizes and order of approximations for efficient numerical simulations. The computational cost of complex simulations can be optimized by adapting the mesh or polynomial degrees, in different regions of solutions. For example, in the region close to the inlet boundaries, the time-dependent inlet velocity would generate oscillations when it keeps increasing or decreasing before reaching a steady-state. Besides, the suddenly added inlet velocity or stopped inlet velocity would also generate high jump of solutions, so it necessary to adopt adaptive mesh refinement in these specific regions in order to have smooth solutions[67].

7.2.3 Boost of performance

This is always a hot topic and important step in large scale scientific computing. Although the code in Femuss is written in Fortran and can be run in multi-processors, there are may still many other special techniques to boost the performance. Recalling the existed two groups of domain de-composition

methods,i.e, overlapping and non-overlapping domain de-composition, we can chose one of them according to the size of our problem. More precisely, with different domain de-composition methods such as Dirchlet-Neumann, Neumann-Neumann, Balanced Neumann-Neumann and Balanced Neumann-Neumann by constraint, the linear system equations to be solved would have different condition number, making the problem strong scalable or weak scalable[68, 69].

Appendix A

Properties of dust particles

Particle size	$1 \cdot 10^{-1}\mathrm{m}$
Particle surface wetness	0.02
Particle plastic pressure	$1000\mathrm{Pa}$
Air density	$1.18\mathrm{kg} \cdot \mathrm{m}^{-3}$
Dynamic Viscosity of air	$1.8 \cdot 10^{-5}\mathrm{Pa} \cdot \mathrm{s}$
Vegetated fraction	0
Particle density	$2.5 \cdot 10^{-1}\mathrm{kg} \cdot \mathrm{m}^{-3}$
Bare roughness	0.002
Gravity	$9.81\mathrm{kg} \cdot \mathrm{m} \cdot \mathrm{s}^{-2}$

Bibliography

[1] Jung Y Kang et al. "Comparison of vertical dust flux by implementing three dust emission schemes in WRF/Chem". In: *Journal of Geophysical Research Atmospheres* 116.9 (2011), pp. 1–18. ISSN: 01480227. DOI: 10.1029/2010JD014649.

[2] H Lu and Y Shao. "Toward quantitative prediction of dust storms: An integrated wind erosion modelling system and its applications". In: *Environmental Modelling and Software* 16.3 (2001), pp. 233–249. ISSN: 13648152. DOI: 10.1016/S1364-8152(00)00083-9.

[3] H. N. Lee et al. "Long range transport of Asian dust from dust storms and its impact on Japan". In: *Water, Air, and Soil Pollution: Focus* 3.2 (2003), pp. 231–243. ISSN: 15677230. DOI: 10.1023/A:1023254910362.

[4] M Stovern et al. "Simulation of windblown dust transport from a mine tailings impoundment using a computational fluid dynamics model". In: *Aeolian Research* 14 (2014), pp. 75–83. ISSN: 18759637. DOI: 10.1016/j.aeolia.2014.02.008. URL: http://dx.doi.org/10.1016/j.aeolia.2014.02.008.

[5] A Mogilner and L Edelstein-Keshet. "Regulation of actin dynamics in rapidly moving cells: a quantitative analysis". In: *Biophysical journal* 83.3 (2002), pp. 1237–1258.

[6] JR Thompson et al. "The effect of dust on photosynthesis and its significance for roadside plants". In: *Environmental Pollution Series A, Ecological and Biological* 34.2 (1984), pp. 171–190.

[7] JH Vincent and D Mark. "Applications of blunt sampler theory to the definition and measurement of inhalable dust". In: *Inhaled Particles V: Proceedings of an International Symposium Organized by the British Occupational Hygiene Society, Cardiff, 8-12 September 1980*. Vol. 26. Elsevier. 2013, p. 0.

[8] Norbert Englert. "Fine particles and human health? a review of epidemiological studies". In: *Toxicology letters* 149.1 (2004), pp. 235–242.

[9] D Giannadaki, A Pozzer, and J Lelieveld. "Modeled global effects of airborne desert dust on air quality and premature mortality". In: *Atmospheric Chemistry and Physics* 14.2 (2014), pp. 957–968.

[10] B Brunekreef and B Forsberg. "Epidemiological evidence of effects of coarse airborne particles on health". In: *European Respiratory Journal* 26.2 (2005), pp. 309–318.

[11] A Nel. "Air pollution-related illness: effects of particles". In: *Science* 308.5723 (2005), pp. 804–806.

[12] K Pye. *Aeolian dust and dust deposits*. Elsevier, 2015.

[13] M Dall'Osto et al. "Variation of the mixing state of Saharan dust particles with atmospheric transport". In: *Atmospheric Environment* 44.26 (2010), pp. 3135–3146.

[14] G Rubasinghege et al. "Reactions on atmospheric dust particles: surface photochemistry and size-dependent nanoscale redox chemistry". In: *The Journal of Physical Chemistry Letters* 1.11 (2010), pp. 1729–1737.

[15] Arthur C Stern. *Fundamentals of air pollution*. Elsevier, 2014.

[16] D Gillette and Paul A Goodwin. "Microscale transport of sand-sized soil aggregates eroded by wind". In: *Journal of Geophysical Research* 79.27 (1974), pp. 4080–4084.

[17] F Pasquill. "Atmospheric Diffusion, (1974)". In: *Wiley* 17 (1962), p. 429.

[18] MHA Hassan and IA Eltayeb. "Suspension transport of wind-eroded sand particles". In: *Geophysical Journal International* 104.1 (1991), pp. 147–152.

[19] Ibrahim A Eltayeb and MHA Hassan. "Two-dimensional transport of dust from an infinite line source at ground level". In: *Geophysical Journal International* 110.3 (1992), pp. 571–576.

[20] Jason A Roney and Bruce R White. "Comparison of a two-dimensional numerical dust transport model with experimental dust emissions from soil surfaces in a wind tunnel". In: *Atmospheric Environment* 44.4 (2010), pp. 512–522. ISSN: 13522310. DOI: 10.1016/j.atmosenv.2009.10.046. URL: http://dx.doi.org/10.1016/j.atmosenv.2009.10.046.

[21] Ralph A Bagnold. "Physics of blown sand and sand dunes". In: *William Morrow and Co., New York* (1941).

[22] R Greeley and JD Iversen. "Wind as a geological process on Earth, Mars, Venus and Titan." In: *Wind as a geological process on Earth, Mars, Venus and Titan.. R. Greeley, JD Iversen. Cambridge Planetary Science Series, Vol. 4. Cambridge University Press, Cambridge-London-New York-New Rochelle-Melbourne-Sydney. 12+ 333 pp. Price DM 147.50 (1985). ISBN0-521-24385-8.* 1 (1985).

[23] M Phillips. "A force balance model for particle entrainment into a fluid stream". In: *Journal of Physics D: Applied Physics* 13.2 (1980), p. 221.

[24] YP Shao and H Lu. "A simple expression for wind erosion threshold friction velocity". In: *Journal of Geophysical Research: Atmospheres* 105.D17 (Sept. 2000), pp. 22437–22443. ISSN: 01480227. DOI: 10.1029/2000JD900304. URL: http://doi.wiley.com/10.1029/2000JD900304.

[25] YP Shao, Michael R Raupach, and John F Leys. "A model for predicting aeolian sand drift and dust entrainment on scales from paddock to region". In: *Soil Research* 34.3 (1996), pp. 309–342.

[26] F Fécan, B Marticorena, and G Bergametti. "Parametrization of the increase of the aeolian erosion threshold wind friction velocity due to soil moisture for arid and semi-arid areas". In: *Annales Geophysicae*. Vol. 17. 1. Springer. 1998, pp. 149–157.

[27] TL Zhao et al. "An assessment of dust emission schemes in modeling east Asian dust storms". In: *Journal of Geophysical Research: Atmospheres* 111.D5 (2006).

[28] K. Haustein et al. "Testing the performance of state-of-the-art dust emission schemes using DO4Models field data". In: *Geoscientific Model Development* 8.2 (2015), pp. 341–362. ISSN: 19919603. DOI: 10.5194/gmd-8-341-2015.

[29] MR Raupach, DA Gillette, and JF Leys. "The effect of roughness elements on wind erosion threshold". In: *Journal of Geophysical Research: Atmospheres* 98.D2 (1993), pp. 3023–3029.

[30] K Darmenova et al. "Development of a physically based dust emission module within the weather research and forecasting (WRF) model: Assessment of dust emission parameterizations and input parameters for source regions in central and east asia". In: *Journal of Geophysical Research Atmospheres* 114.14 (2009), pp. 1–28. ISSN: 01480227. DOI: 10.1029/2008JD011236.

[31] B Marticorena et al. "Surface and aerodynamic roughness in arid and semiarid areas and their relation to radar backscatter coefficient". In: *Journal of Geophysical Research: Earth Surface* 111.F3 (2006).

[32] JF Leys. "Towards a better model of the effect of prostrate vegetation cover on wind erosion". In: *Vegetation and climate interactions in semi-arid regions*. Springer, 1991, pp. 49–58.

[33] L Gomes et al. "Validation of a dust production model from measurements performed in semi-arid agricultural areas of Spain and Niger". In: *Catena* 52.3 (2003), pp. 257–271.

[34] YP Shao, MR Raupach, and PA Findlater. "Effect of saltation bombardment on the entrainment of dust by wind". In: *Journal of Geophysical Research: Atmospheres* 98.D7 (1993), pp. 12719–12726.

[35] D Ono. "Application of the Gillette model for windblown dust at Owens Lake, CA". In: *Atmospheric Environment* 40.17 (2006), pp. 3011–3021. ISSN: 13522310. DOI: 10.1016/j.atmosenv.2005.08.048.

[36] R Kawamura. "Study of sand movement by wind. Hydraulics Engineering Laboratory Report HEL-2-8". In: *University of California, Berkeley* (1951), p. 38.

[37] JN Svasek and JHJ Terwindt. "Measurements of sand transport by wind on a natural beach". In: *Sedimentology* 21.2 (1974), pp. 311–322.

[38] Bruce R White. "Soil transport by winds on Mars". In: *Journal of Geophysical Research: Solid Earth* 84.B9 (1979), pp. 4643–4651.

[39] P Rr Owen. "Saltation of uniform grains in air". In: *Journal of Fluid Mechanics* 20.02 (1964), pp. 225–242.

[40] W Chen and Donald W Fryrear. "Aerodynamic and geometric diameters of airborne particles". In: *Journal of Sedimentary Research* 71.3 (2001), pp. 365–371.

[41] M Sørensen. "On the rate of aeolian sand transport". In: *Geomorphology* 59.1-4 (Apr. 2004), pp. 53–62. ISSN: 0169555X. DOI: 10.1016/j.geomorph.2003.09.005. URL: http://linkinghub.elsevier.com/retrieve/pii/S0169555X03003131.

[42] B Marticorena and G Bergametti. "Modeling the atmospheric dust cycle: 1. Design of a soil-derived dust emission scheme". In: *Journal of Geophysical Research: Atmospheres* 100.D8 (1995), pp. 16415–16430.

[43] B Marticorena et al. "Modeling the atmospheric dust cycle: 2. Simulation of Saharan dust sources". In: *Journal of Geophysical Research: Atmospheres* 102.D4 (1997), pp. 4387–4404.

[44] B Laurent et al. "Modeling mineral dust emissions from Chinese and Mongolian deserts". In: *Global and Planetary Change* 52.1 (2006), pp. 121–141.

[45] YP Shao. *Physics and modelling of wind erosion*. Vol. 37. Springer Science & Business Media, 2008.

[46] H Lu and YP Shao. "A new model for dust emission by saltation". In: *J. Geophys. Res* 104 (1999), pp. 16827–16842.

[47] YP Shao. "A model for mineral dust emission". In: *Journal of Geophysical Research: Atmospheres* 106.D17 (2001), pp. 20239–20254.

[48] YP Shao. "Simplification of a dust emission scheme and comparison with data". In: *Journal of Geophysical Research* 109.D10 (2004), p. D10202. ISSN: 0148-0227. DOI: 10.1029/2003JD004372. URL: http://doi.wiley.com/10.1029/2003JD004372.

[49] AL Kholodenko and JF Douglas. "Generalized Stokes-Einstein equation for spherical particle suspensions". In: *Physical Review E* 51.2 (1995), p. 1081.

[50] R Codina. "Comparison of some finite element methods for solving the diffusion-convection-reaction equation". In: *Comput. Methods Appl. Mech. Engrg* 156.97 (1998), pp. 185–210. ISSN: 00457825. DOI: 10.1016/S0045-7825(97)00206-5.

[51] Alexander N Brooks and Thomas JR Hughes. "Streamline upwind/Petrov-Galerkin formulations for convection dominated flows with particular emphasis on the incompressible Navier-Stokes equations". In: *Computer methods in applied mechanics and engineering* 32.1-3 (1982), pp. 199–259.

[52] Thomas JR Hughes, Leopoldo P Franca, and Gregory M Hulbert. "A new finite element formulation for computational fluid dynamics: VIII. The Galerkin/least-squares method for advective-diffusive equations". In: *Computer Methods in Applied Mechanics and Engineering* 73.2 (1989), pp. 173–189.

[53] Thomas JR Hughes. "Multiscale phenomena: Green's functions, the Dirichlet-to-Neumann formulation, subgrid scale models, bubbles and the origins of stabilized methods". In: *Computer methods in applied mechanics and engineering* 127.1-4 (1995), pp. 387–401.

[54] Leopoldo P Franca and C Farhat. "Bubble functions prompt unusual stabilized finite element methods". In: *Computer Methods in Applied Mechanics and Engineering* 123.1-4 (1995), pp. 299–308.

[55] J Douglas and JP Wang. "An absolutely stabilized finite element method for the Stokes problem". In: *Mathematics of computation* 52.186 (1989), pp. 495–508.

[56] R Codina. "Finite element approximation of the convection-diffusion equation: Subgrid-scale spaces, local instabilities and anisotropic space-time discretizations". In: *Lecture Notes in Computational Science and Engineering* 81 LNCSE (2011), pp. 85–97. ISSN: 14397358. DOI: 10.1007/978-3-642-19665-2_10.

[57] F Brezzi and M Fortin. *Mixed and hybrid finite element methods*. Vol. 15. Springer Science & Business Media, 2012.

[58] R Codina. "Stabilized finite element approximation of transient incompressible flows using orthogonal subscales". In: *Computer Methods in Applied Mechanics and Engineering* 191.39-40 (2002), pp. 4295–4321. ISSN: 00457825. DOI: 10.1016/S0045-7825(02)00337-7.

[59] C Bayona, J Baiges, and R Codina. "Variational multi-scale finite element solution of the compressible Navier-Stokes equations". In: *International Journal of Numerical Methods for Heat & Fluid Flow* 26.3/4 (2015), pp. 1–42. DOI: 10.1108/HFF-11-2015-0483. URL: http://www.emeraldinsight.com/doi/full/10.1108/HFF-11-2015-0483.

[60] R Codina. "A discontinuity-capturing crosswind-dissipation for the finite element solution of the convection-diffusion equation". In: *Computer Methods in Applied Mechanics and Engineering* 110.3-4 (1993), pp. 325–342.

[61] Jim J Lin, Kenneth E Noll, and Thomas M Holsen. "Dry Deposition Velocities as a Function of Particle Size in the Ambient Atmosphere Dry Deposition Velocities as a Function of Particle Size in the Ambient Atmosphere". In: *Aerosol Science and Technology* 20.3 (2016), pp. 1521–7388. ISSN: 0278-6826. DOI: 10.1080/02786829408959680. URL: http://www.tandfonline.com/action/journalInformation?journalCode=uast20{\%}5Cnhttp://dx.doi.org/10.1080/02786829408959680.

[62] Jason A Roney and Bruce R White. "Estimating fugitive dust emission rates using an environmental boundary layer wind tunnel". In: 40 (2006), pp. 7668–7685. DOI: 10.1016/j.atmosenv.2006.08.015.

[63] Robert G Bryant. "Recent advances in our understanding of dust source emission processes". In: *Progress in Physical Geography* 37.3 (2013), pp. 397–421.

[64] D Goossens and Brenda J Buck. "Can BSNE (Big Spring Number Eight) samplers be used to measure PM10, respirable dust, PM2. 5 and PM1. 0?" In: *Aeolian Research* 5 (2012), pp. 43–49.

[65] E Teper. "Dust-particle migration around flotation tailings ponds: pine needles as passive samplers". In: *Environmental monitoring and assessment* 154.1 (2009), pp. 383–391.

[66] B. Shannak et al. "Wind tunnel study of twelve dust samples by large particle size". In: *Atmospheric Environment* 98 (2014), pp. 442–453. ISSN: 18732844. DOI: 10.1016/j.atmosenv.2014.08.062. URL: http://dx.doi.org/10.1016/j.atmosenv.2014.08.062.

[67] J Donea and A Huerta. *Finite element methods for flow problems*. John Wiley & Sons, 2003.

[68] S Badia, Alberto F Martín, and J Principe. "A highly scalable parallel implementation of balancing domain decomposition by constraints". In: *SIAM Journal on Scientific Computing* 36.2 (2014), pp. C190–C218.

[69] S Badia, Alberto F Martín, and J Principe. "Implementation and scalability analysis of balancing domain decomposition methods". In: *Archives of Computational Methods in Engineering* 20.3 (2013), pp. 239–262.